INVESTIGATION OF WAVE LOADS AT THE LEE-SIDE OF A RUBBLE MOUND BREAKWATER HEAD

A THESIS SUBMITTED TO
THE GRADUATE SCHOOL OF NATURAL AND APPLIED SCIENCES
OF
MIDDLE EAST TECHNICAL UNIVERSITY

BY

CEM SEVİNDİK

IN PARTIAL FULFILLMENT OF THE REQUIREMENTS
FOR
THE DEGREE OF MASTER OF SCIENCE
IN
CIVIL ENGINEERING

SEPTEMBER 2023

Approval of the thesis:

INVESTIGATION OF WAVE LOADS AT THE LEE-SIDE OF A RUBBLE MOUND BREAKWATER HEAD

submitted by **CEM SEVİNDİK** in partial fulfillment of the requirements for the degree of **Master of Science in Civil Engineering, Middle East Technical University** by,

Prof. Dr. Halil Kalıpçılar
Dean, Graduate School of **Natural and Applied Sciences**

Prof. Dr. Erdem Canbay
Head of the Department, **Civil Engineering**

Assist. Prof. Dr. Cüneyt Baykal
Supervisor, **Civil Engineering, METU**

Dr. Hasan Gökhan Güler
Co-Supervisor, Civil Engineering**, METU**

Examining Committee Members:

Assist. Prof. Dr. Gülizar Özyurt Tarakcıoğlu
Civil Engineering, METU

Assist. Prof. Dr. Cüneyt Baykal
Civil Engineering, METU

Prof. Dr. Veysel Şadan Özgür Kırca
Civil Engineering, ITU

Prof. Dr. Kubilay Cihan
Civil Engineering, KKU

Assist. Prof. Dr. Doğan Kısacık
Civil Engineering, IZTECH

Date: 08.09.2023

I hereby declare that all information in this document has been obtained and presented in accordance with academic rules and ethical conduct. I also declare that, as required by these rules and conduct, I have fully cited and referenced all material and results that are not original to this work.

Name Last name : Cem Sevindik

Signature :

ABSTRACT

INVESTIGATION OF WAVE LOAD AT THE LEE-SIDE OF A RUBBLE MOUND BREAKWATER HEAD

Sevindik, Cem
Master of Science, Civil Engineering
Supervisor: Asst. Prof. Dr. Cüneyt Baykal
Co-Supervisor: Dr. Hasan Gökhan Güler

September 2023, 92 pages

It is well-known that head sections of the rubble mound breakwaters are more critical than trunk sections in terms of stability. The common practice is to use heavier armor layer units at the head sections of rubble mound breakwaters, especially at the lee-side of the head sections. However, the relation between the wave parameters and hydrodynamic loading at the lee-side of the head section has not been completely investigated.

In the scope of this study, physical model experiments were conducted to observe the relation between the wave parameters and hydrodynamic loading at the lee-side of the head section of a rubble mound breakwater constructed using antifer units. The experiments were carried out at the Coastal and Ocean Engineering Laboratory of the METU Civil Engineering Department. The armor layer slope of the tested physical model was 1:1.5, and antifer units were placed on both the head and trunk sections of the breakwater. In the experiments, 8 different water depths, 13 different wave periods, and a single wave steepness value of 0.045 were considered. During the experiments, pressure measurements on the top face of a single antifer unit at the lee-side of the head section were carried out in addition to water surface elevation and particle velocity measurements at different locations along the wave flume and around the cross-section.

According to the results, during the passage of a single wave, hydrodynamic loading on a single antifer unit changes remarkably depending on the presence and location of wave-breaking. It is observed that the pressure signal on the top face of the unit takes a double-peaked form rather than single-peaked with strong negative dynamic pressure values when the plunger breaks at an average circumferential distance of 1.08 unit width offshore and vertical distance of 0.61 unit width above. Furthermore, velocities significantly increase closer to the lee-side of the head section up to three times the undisturbed values.

Keywords: Breakwater, Head, Lee-side, Wave Load Measurement, Signal Processing

ÖZ

TAŞ DOLGU DALGAKIRAN MÜZVARININ LİMAN TARAFINDAKİ DALGA YÜKLERİ ÜZERİNE BİR ARAŞTIRMA

Sevindik, Cem
Yüksek Lisans, İnşaat Mühendisliği
Tez Yöneticisi: Dr. Öğr. Üyesi Cüneyt Baykal
Ortak Tez Yöneticisi: Dr. Hasan Gökhan Güler

Eylül 2023, 92 sayfa

Taş dolgu dalgakıranların müzvar kısmının stabilite açısından gövde kısmına göre daha kritik olduğu bilinmektedir. Yaygın olan uygulama, taş dolgu dalgakıranların müzvar kısmında, özellikle müzvar kısmının liman tarafında daha ağır koruyucu tabaka elemanlarının kullanılmasıdır. Ancak müzvar kısmının liman tarafında dalga parametreleri ile hidrodinamik yükleme arasındaki ilişki tam olarak araştırılmamıştır.

Bu çalışmanın kapsamında, antifer birimler kullanılarak inşa edilen bir taş dolgu dalgakıranın müzvar kısmının liman tarafında dalga parametreleri ve hidrodinamik yükleme arasındaki ilişkiyi gözlemlemek için deneysel bir çalışma yapılmıştır. Deneyler ODTÜ İnşaat Mühendisliği Bölümü Kıyı ve Deniz Mühendisliği Laboratuvarı'nda gerçekleştirilmiştir. Test edilen fiziksel modelin koruma tabakası eğimi 1:1,5 olup, antifer birimleri dalgakıranının hem müzvar hem de gövde kısımlarına yerleştirilmiştir. Deneylerde 8 farklı su derinliği, 13 farklı dalga periyodu ve 0,045'lik tek bir dalga dikliği değeri dikkate alınmıştır. Deneyler sırasında, dalga kanalı boyunca ve kesit çevresinde farklı noktalarda su yüzeyi yüksekliği ve parçacık hızı ölçümlerine ek olarak, müzvar kısmının liman tarafında tek bir antifer biriminin üst yüzeyinde basınç ölçümleri gerçekleştirilmiştir.

Sonuçlara göre, tek bir dalganın geçişi sırasında, bir antifer biriminin üzerindeki hidrodinamik yükleme, dalga kırılmasının olmasına ve konumuna bağlı olarak önemli ölçüde değişiklik göstermektedir. Dalganın sensöre ortalama 1,08 birim genişlikte çevresel mesafede ve ortalama 0,61 birim genişlikte düşey mesafede kırılması durumunda, antifer ünitesi üzerinde okunan basınç sinyalinin güçlü negatif dinamik basınç değerleri ile tek tepeli yerine çift tepeli bir şekil aldığı görülmektedir. Ayrıca, hızlar müzvar kısmının liman tarafına yaklaştıkça, yapıdan uzaktaki hız değerlerinin üç katına kadar önemli ölçüde artmaktadır.

Anahtar Kelimeler: Dalgakıran, Müzvar, Liman Tarafı, Dalga Yükü Ölçümleri, Sinyal İşleme

To Mustafa Kemal ATATÜRK, the savior and eternal hero of the Turkish nation

ACKNOWLEDGMENTS

I would like to express my sincere gratitude to my thesis supervisor Asst. Prof. Dr. Cüneyt Baykal for his guidance, patience, valuable suggestions, and support at any time of the day. Without his valuable help, this study would not have been possible to be carried out and I would not have been able to improve myself. It was a great chance for me to work with him.

I would like to express my sincere gratitude to my thesis co-supervisor Dr. Hasan Gökhan Güler for his ideas, solutions, patience, and precious help. His comforting attitude and support even in the most difficult moments were one of the effective factors in completing this study. Working with him was a great chance and experience.

I would like to express my sincere gratitude to my instructor, boss, and one of my idols Dr. Işıkhan Güler for his guidance and valuable suggestions. He has greatly influenced my decision on what kind of coastal engineer I want to be. Working with him was a great experience.

I would like to express my sincere gratitude to Prof. Dr. Ayşen Ergin, Prof. Dr. Ahmet Cevdet Yalçıner, Asst. Prof. Dr. Gülizar Özyurt Tarakcıoğlu and Dr. Gözde Güney Doğan Bingöl for the education and knowledge that I received from them. It was a priceless chance to get to know them and learn from them.

I would like to thank my colleagues and friends Furkan Demir and Günay Gazaloğlu, who supported my experimental studies by spending sleepless nights with me. I wish endless success to these two people, who are like brothers to me, in Plymouth. It is impossible to repay their efforts during the experiment process and my thesis study.

I would like to thank my colleagues and friends Barış Ufuk Şentürk, Berkay Erler, and Mert Yaman, who have always supported me and stood by me. Thanks to their help, I have found the motivation to finish this study. It is impossible to repay their efforts during the experiment process and my thesis study. I am glad to have such brothers. I wish endless success to them.

I would like to thank my dear friends Akdeniz İnce, Alperen Korkmaz, Arif Çağatay Uysal, Berkay Akyol Bilge Karakütük, Elif Ayşe Öztürk, İrem Naz Kösem, Irmak Öztürk, and Yağız Arda Çiçek for their supports and friendship. I am lucky to have known them.

I would like to thank Yusuf Korkut for his endless help during the construction of the physical model. Without his help, it would have been very difficult to complete the physical model experiments. I would like to express my thanks to Nuray Çimen and Ayhan Karadeniz for their support and kindness.

I would like to thank my boss Yasemin Özgen, Can Öcal, Saygın Kemal Derebay, and my other colleagues at Dolfen Consulting and Engineering Company for their support and patience for my excuses.

I would like to thank my grandmother Zehra Sevindik, and my grandfather Mesut Sevindik who passed away two years ago, for their support. I feel fortunate to be their grandson.

I would like to thank my grandmother Nurhan Akdoğan, my grandfather - first and best friend Hamdi Akdoğan, my uncle Mutlu Akdoğan, my aunts Feray Başaran and Günay Akdoğan, my aunt-in-law Melek Akdoğan and my uncle-in-law Ali Yusuf Başaran for their support and kindness. I would also thank to my dear cousins Deniz Akdoğan, Eylül Akdoğan, and Zehra Başaran, whom I see as my brothers and sisters. I feel fortunate to have such a family. I am glad they are in my life.

I would like to thank my dearest friend Elif Ezgi Ceylan who has always supported me and stood by me. I am lucky to have known her. I am grateful for her patience and kindness during the hardships I faced, during this study.

I would like to express my deepest thanks and gratitude to my mother Zeynep Sevindik. I have found the patience and strength that I needed to conduct my master's degree study with her support and the motivation that she gave me. Having such a mother is one of the biggest chances in my life.

Last but not least, I would like to express my deepest thanks and gratitude to my father Ali Ulvi Sevindik, who is my first idol and the biggest factor in choosing my profession, for introducing me to coastal engineering. It is a great pleasure to be colleagues with him and to be able to ask him every question I have in my mind about my profession.

TABLE OF CONTENTS

LIST OF TABLES

TABLES

LIST OF FIGURES

FIGURES

LIST OF ABBREVIATIONS

ABBREVIATIONS

ADV	Acoustic Doppler velocimetry
AYGM	Altyapı Yatırımları Genel Müdürlüğü
BIOR	Biorthogonal spline wavelet
CFD	Computational fluid dynamics
CIRIA	Construction Industry Research and Information Association
COIF	Coiflet wavelet
DB	Daubechies wavelet
DMEY	Discrete approximation of Meyer wavelet
FIR	Finite impulse response
FK	Fejer-Krovkin wavelet
GRU	Gated recurrent unit
HAAR	Haar Wavelet
KC	Keulegan-Carpenter number
LDV	Laser Doppler velocimetry
LSTM	Long short-term memory
MAE	Mean absolute error
METU	Middle East Technical University
MSE	Mean squared error
MLP	Multi-layer perceptron

N-MAE	Normalized mean absolute error
N-MSE	Normalized mean squared error
OpenFOAM	Open-source Field Operation and Manipulation
R	Pearson’s linear correlation coefficient
RANS	Reynolds averaged Navier-Stokes
RBIO	Reverse biorthogonal spline wavelet
RF	Random forest
SI	Scatter index
SVR	Support regression vector
SWL	Still water level
SYM	Symlet wavelet
USACE	United States Army Corps for Engineers
WG	Wave gauge

LIST OF SYMBOLS

SYMBOLS

α	Angle of breakwater armor slope
ρ	Density of water
ν	Kinematic viscosity
d	Water depth
g	Gravitational acceleration
h	Water depth
H	Wave height
L	Wave length
m	Bed slope
T	Wave period
P_{max}	Maximum pressure values of the first peak of double-peaked hydrodynamic loading type
P_{min}	Minimum pressure values of the first peak of double-peaked hydrodynamic loading type
ΔP	Absolute differences of maximum and minimum pressure values of the first peak of double-peaked hydrodynamic loading types
ΔX	Circumferential offshore distance in terms of base length of an antifer
ΔZ	Vertical distance in terms of base length of an antifer

CHAPTER 1

INTRODUCTION

1.1 Motivation

Breakwaters are one of the most important types of coastal structures and are generally constructed to create protected berthing areas for commercial and leisure activities and beach restoration. The most widely used type of breakwater is rubble mound breakwater (Ergin, 2019) in Turkey and Europe.

Today, many empirical equations are used for rubble mound breakwaters and these principles determine a design methodology based on the weight and volume of the rock material or other artificial concrete armor layer units, although there is no design methodology on the forces and pressures of waves and wave breaking on the armor layer units. Another important point is the formation of a series of vortices after wave breaking. After waves break on the head section of a rubble mound breakwater, vortex formation is observed, and the formation steps of these vortices are relatively known. However, the hydrodynamic force and effect of the vortex formations on the armor layer units are not known.

Using heavier rock or artificial armor layer units is a general practice at the head section of a rubble mound breakwater as this section is more critical than the trunk section in terms of stability because of high cone-overflow velocities generated by wave refraction, wave breaking, and decreased support of neighboring units (CIRIA et al., 2007; USACE, 2011). It is known and highlighted in several references that the lee-side of the rubble mound breakwater head faces excessive damage more than the other parts of the head section. However, the relation between the wave-breaking-induced hydrodynamic loads and wave parameters has not been completely investigated, forming a clear and important literature gap.

1.2 Objectives of the Study

This thesis study focused on the hydrodynamic loads caused by breaking waves at the lee side of the head section of a rubble mound breakwater. To understand these loads on the armor layer, an experimental setup was constructed and pressure, water surface elevation, and velocity measurements were conducted on and around this rubble mound breakwater head physical model under various water level and wave conditions. In the tests, regular waves were used. Video recordings were taken to determine wave breaking type and location at the breakwater head close to the pressure sensor.

This study tries to answer the given research questions below:

i. How does the presence and location of wave breaking affect the hydrodynamic loading at the lee side of the head section of the rubble mound breakwater?

ii. What is the relation between wave parameters (individual wave height, wave period, and breaking type) and wave loads acting on the armor units of the lee-side of the head section of the rubble mound breakwater?

1.3 Contents of the Chapters

This thesis consists of four main chapters besides Chapter 1, the introduction part. The content of the chapters is as follows.

In the second chapter, a literature review that is related to this thesis study is mentioned and related studies are summarized in four parts. In the first part of this chapter, information about wave load measurement on the armor layer of rubble mound breakwaters is discussed. In the second part of Chapter 2, design methodologies on the head section of rubble mound breakwaters are given. Furthermore, in the following parts, experimental studies on head sections of rubble mound breakwaters and short-wave breaking vortices are summarized, separately.

In the third chapter, the methodology of the whole study is mentioned in six parts. In the first part of this chapter, the experimental setup is explained in detail. In the second part, information on how the parameters were determined in the experiments and how the measurements were taken was given. Since there is noise in the data obtained from velocity and pressure measurements, it was necessary to filter the data. In the third part, this signal-filtering process is mentioned. In the error analysis part, the studies were carried out to find the best filter to eliminate the noise present in the velocity and pressure measurements obtained from the experiments. In the fifth part, information about non-dimensional analysis studies and used parameters are explained and in the sixth part, the data analysis part is briefly mentioned.

In the fourth chapter, the results of the experimental studies and necessary discussions on these results are given.

In the fifth chapter, the conclusion of this thesis study is given. Suggestions for further studies on this topic are mentioned in this chapter, as well.

Finally, as the last part of this thesis, a detailed explanation of signal filtering, error analysis procedure on different signal filtering types, and results of the ADV measurements that are mentioned in Chapter 3 are given in Appendices A, B, and C, respectively.

CHAPTER 2

LITERATURE REVIEW

In the scope of this thesis study, wave loadings and pressures due to wave breaking were investigated on the lee side of the head section of a rubble mound breakwater physical model. For the literature review, part of the study, wave load measurements on the armor layer of rubble mound breakwaters, design methodologies of the lee-side of the head section of rubble mound breakwaters, experimental studies on rubble mound breakwater head sections, and experimental studies on the formation of vortices were reviewed and summarized.

2.1 Measuring Wave Loads on the Armor Layer

There are several pressure measurement studies conducted on the armor layer of rubble mound breakwaters. In this section, related studies about this topic are mentioned.

Sandstrøm (1974) carried out an experimental study to determine the variations in the wave-induced forces on a rubble mound breakwater armor layer. On the slope, sphere units were used to represent idealized stone. In these experiments, regular waves were applied to the model, and measurements were recorded by strain gauges that were placed on the sphere units.

Iwata et al. (1985) carried out an experimental study to investigate the wave forces that act on the rock units that were placed on the armor layer of a rubble mound breakwater. The measurements that were carried out for the wave forces, were conducted directly. Then, these measured forces were decomposed into two forces that are drag force and inertial force. Characteristics of these forces and their coefficient values were analyzed.

Losada et al. (1988) conducted an experimental study to measure the hydrodynamic forces on the armor layer. For this purpose, a cubic block armor layer unit was used and it was placed near the bottom part of the physical model. During the experiments, both horizontal and vertical components of the solitary wave-induced forces were investigated. Furthermore, in the scope of this study, hydrodynamic coefficients such as drag and inertia coefficients, were determined for varying boundary conditions.

Sakakiyama and Kajima (1990) carried out an experimental study to investigate the scale effect on the armor layer unit stability in terms of wave-induced forces. For this purpose, three experiments were conducted with varying sizes of tetrapod armor layer units to determine the acting wave forces on these units, determine the inertia, and drag coefficients. According to the results of these experiments, it was found that wave force measurements have relatively larger values in small-scale rather than large-scale cases. Another point is that the scale effect on acting wave force on tetrapod units is mainly caused by changes in the relative number of drag forces.

Williamson and Hall (1992) investigated external pressures caused by attacking waves on the front slope of a rubble mound breakwater. Three different armor layer slopes which are 1:1.5, 1:2, and 1:3 were constructed for the experiments and the experiments were carried out by using regular waves up to 30 cm. In the scope of this study, the relation between the parameters such as core permeability, armor layer slope, wave height, and period was tried to be examined.

Tørum (1994) carried out an experimental study to measure the wave forces acting on an armor layer unit on a berm-type breakwater and particle velocity around this armor layer unit by using Laser Doppler Velocimetry (LDV). These measurements were conducted on the flattened part of this reshaped physical model. By using a least square method, coefficients for inertial and drag forces were determined. It was observed that the drag force is the dominant force around the measurement point.

Wise (1999) developed a numerical to predict the acting wave forces on an artificial armor layer unit, which is called A-jacks. The forces that the model predicted can be listed as, buoyancy force, drag force, inertia force, and slamming force due to the penetration of the unit., This numerical model predicted wave forces by determining the rigid body motion of the artificial unit. In the scope of this study, experimental tests were carried out to verify the results that were gathered from this numerical model in the preliminary stage.

Another example of pressure and force measurements on rubble mound breakwaters is that Eden et al. (2019) carried out an experimental study to study the impact of waves on Core-Loc ™ concrete artificial armor layer units. For this purpose, six pressure sensors were mounted in a 3D printed Core-Loc ™ unit and this unit was placed on an impermeable rigid slope which represents the trunk section of a rubble mound breakwater, in a wave flume. This unit was placed on changing locations on the slope and the hydrodynamic loading caused by waves was investigated by studying a wide range of wave conditions, such as wave height, and wave period. In the scope of this study, both regular and irregular wave sets were applied to the physical model.

2.2 Breakwater Head Design

For the design of the rubble mound breakwaters, separate design methodologies for the constituent parts of these structures are included in various technical guidelines and regulations. When the design of the head section and the design of the lee-side of the head section are considered, CIRIA et al. (2007) and USACE (2011) are widely used as main references. In these design manuals, rather than proposing a formula, it is suggested that 1.5 times heavier rock armor layer units should be placed at the head section than the trunk section. One of the reasons behind this recommendation is that wave breaking, and refraction may cause high-cone overflow velocities at the head section and this situation makes the head section more critical than the trunk section in terms of the stability of the armor layer units. Another reason is that armor layer units have less neighboring support at the head section than at the trunk section. AYGM (2016) also refers to CIRIA et al. (2007) and USACE (2011) for the design of the head section of the rubble mound breakwaters.

2.3 Experimental Studies on Head Sections of RMBW

Since a physical model of a rubble mound breakwater head section was used within the scope of this thesis study, a literature review was also conducted for the experimental studies, which were carried out for head sections. For example for those studies, Fredsøe and Sumer (1997) carried out an experimental study to investigate the scour around the head section of a rubble mound breakwater. Two main mechanisms (steady streaming and plunging wave breaking) which are related to scour processes are identified. It was observed that steady streaming occurs around the round head, and it is responsible for the scouring of a hole and this phenomenon generates in front of the rubble mound breakwater. According to the study, another key mechanism, which is plunging breakers, locally occurs at the head section of the rubble mound breakwater and it is responsible for the scouring of a hole at the lee-side of the head section. In the scope of this study, for protection layer extension, an empirical formula is developed. Below given figure (Figure 2.1) shows the 3D sketch that is given in the article (i.e. Fig. 6 of Fredsoe and Sumer, 1997) of the plunging type wave breaking process at the head section of the breakwater.

In the first frame of this sketch, the over-curling step is shown and this step is seen when the velocity of the crest of the wave is more than the velocity of the trough of the wave. The second frame shows the just before the breaking moment of the wave. At this moment, a clear plunger can be seen. In the third frame, after the wave-breaking process, the breaking plunger creates a round jet and this jet impingement process causes the sand grain mobilization. This situation scours a hole at the lee-side of the breakwater head.

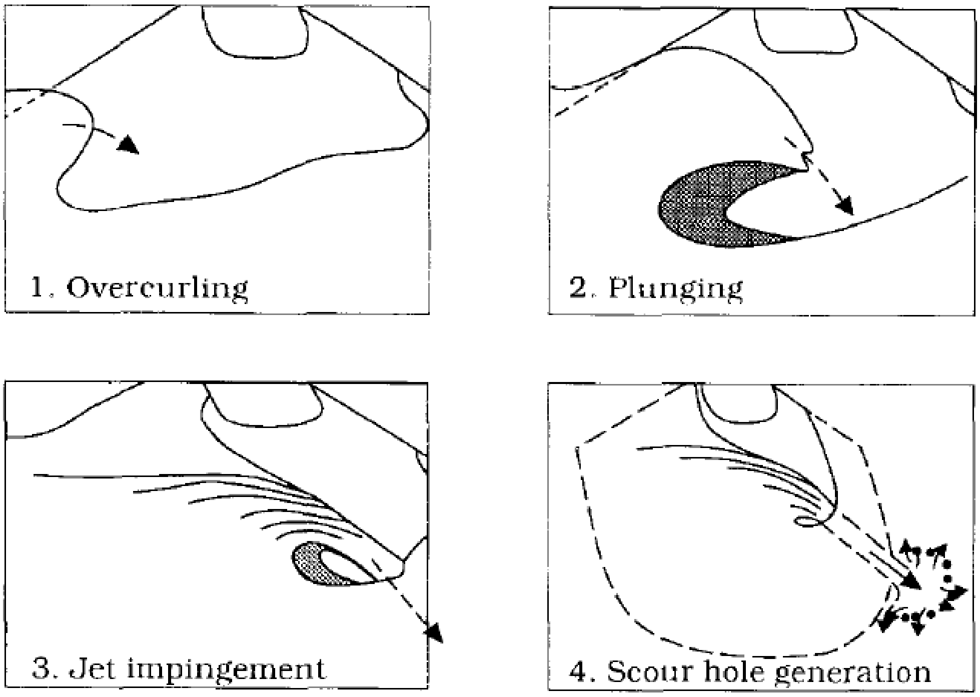

Figure 2.1: 3D Sketch of plunging type wave breaking at the head section (Fredsøe and Sumer, 1997)

As another study example, van Gent (2014) conducted an experimental study on oblique wave attacks on rubble mound breakwaters. For this purpose, a physical model of a rubble mound breakwater was constructed in the wave basin at Deltares, Delft. This constructed physical model included both trunk and head sections. In design methodologies and formulas, wave direction is generally assumed as perpendicular to the coastal structure. In this study, wave directions between perpendicular (0^0) and parallel (90^0) were applied to the constructed model to investigate the stability of cube concrete armor layer units and rock slopes. In the scope of this study, both short and long-crested waves were applied to the physical model.

2.4 Experimental Studies on Short Wave Breaking Vortices

Formation of vortices after wave breaking is a crucial topic for this thesis study and this topic is included in the literature review part. As mentioned in Chapter 1, the formation and structure of vortices after wave breaking over a slope are studied in the literature. In this section, related studies about this topic are mentioned.

Nadaoka et al. (1989) carried out an experimental study to investigate the structure of turbulence in the surf zone and its effect on the dynamics of wave breaking. In the scope of this study, different flow visualization and fiber optic laser Doppler velocimetry (LDV) techniques were used. According to the results, the existence of characteristic structure of eddies in large scales has an important role in the Reynolds stress generation and this causes a deformation of the mean flow field. Another important finding is that these wave-breaking-induced eddies cause vorticity in large amounts into nearly irrotational velocity fields. As a result of this situation, turbulence and also mean flow fields are generated because of this vorticity. Also, it is determined that the formation of wave-breaking induced mean rotational velocity component results in a significant rise in momentum and mass transport, and hence wave height values decrease.

Zhang and Sunamura (1994) carried out 2D wave flume experiments with video recording to investigate multiple bar generation in the light of vortices that are generated by wave breaking. Experiments were carried out in two steps which were fixed-bed and movable-bed experiments. In the fixed-bed experiments, it was found that the generated vortex at the wave breaking location can be categorized into three as two types of horizontal vortices, which are named as A-type and B-type, and oblique formed in the surf zone. Another important finding was that the position of a vortex that reaches the bottom can be defined by bottom slope and wave characteristics, and water depth can be described only by the wave-breaking height. In the movable-bed experiments, it was indicated that the vortices that reach the bottom initiate the formation of bars in the surf zone, and number of vortices matches up with the number of formed bars. Another result of the movable-bed experiments is that two main modes were found in the generation of multiple bars and these are simultaneous and successive modes. The formation of these modes depends on the interaction between the topography and the behavior of the vortex.

Chang et al. (2001) conducted both experimental and numerical studies to investigate the interaction between a submerged obstacle with a rectangular shape and solitary waves. In the scope of this study, the formation and development of vortices, which are because of the flow separation at the corner sides of the submerged rectangular obstacle, are analyzed. The results show that the turbulence intensity of the vortex at the weatherside of the submerged rectangular obstacle is stronger than the turbulence intensity of the vortex at the lee-side however, the size of the formed vortex at the lee-side is larger than that at the weatherside. For the numerical model studies, a Reynolds Averaged Navier-Stokes (RANS) equations based numerical model with a k-ϵ turbulence model was used to verify the results of the experimental measurements. By using this RANS based numerical model, additional numerical studies were carried out by using different wave height values and different sizes of the submerged rectangular shape obstacle in order to find out and examine the significance of the energy dissipation caused by vortices. Chang et al. (2005) conducted the same experimental and numerical studies to investigate the interaction between a submerged obstacle with a rectangular shape by using cnoidal waves. Numerical model studies were carried out to further study the impacts of wave period parameters on the intensity of vortex formation. As the result of this study, it was indicated that fluid turbulence based intensity is closely related with the intensity of vortex.

Sumer et al. (2013) identify the construction process of vortices after wave breaking in detail. In the scope of this study, two parallel laboratory tests were carried out for both bed shear stress measurements on a rigid bed and pore water pressure measurements, morphological change examinations on the bed, and sediment suspension observations on a sediment bed. In this study, it is stated that the formation of a series of vortices is caused by shear layer instability after the plunging type of wave-breaking process. According to the measurement results, it can be noted that peak values of offshore-directed bed shear stresses can be developed by the formed vortices. In addition, the results of pore pressure measurements near the bed show that these vortices may lead to high upward-directed pressure gradients. In the study of Sumer et al. (2013), a detailed sequence of sketches for plunging-type wave breaking is given in Figure 3 in the article. This drawing is also given below in Figure 2.2. The most important feature of this drawing is that this sequence shows the generation of a vortex beneath breaking. This vortex is formed because of the curling of the wave during the breaking process and offshore-directed flow caused by the rundown process after the wave breaking. These reasons are jointly responsible for the formation of Vortex M, which is shown in frame (b) in the drawing. After the formation of Vortex M, two more vortices, which are Vortex N and Vortex P are formed and these are drawn in frames (e) and (f). In general, the formation of these M, N, and P vortices is caused by shear layer instability.

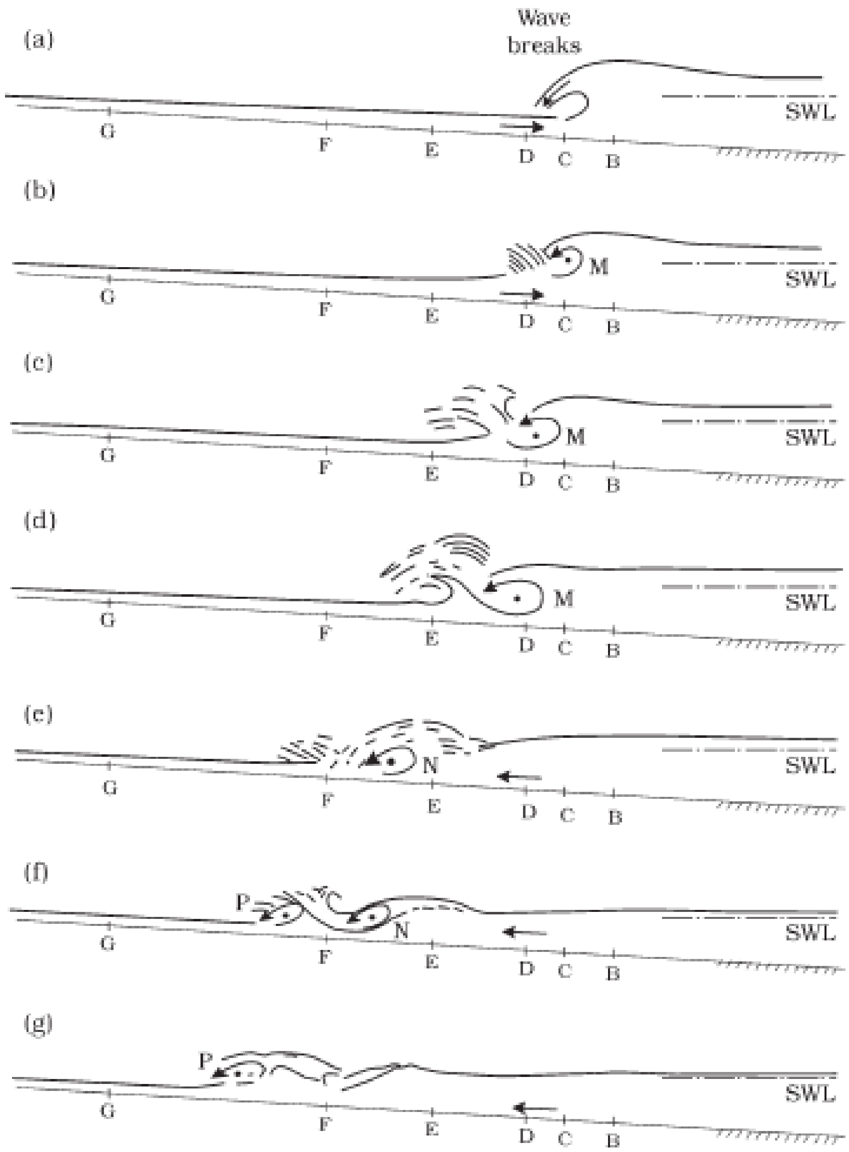

Figure 2.2: Sequence of sketches for plunging type wave breaking

Brocchini et al. (2022) carried out an experimental study to investigate the vortex-vortex interactions. In the experiments, a single regular wave was sent to the discontinuous rigid bed that is responsible for the generation of vortices on the surface and near-bed. It was observed that the flow separation which occurs discontinuity on the be, is responsible for the generation of the near-bed vortices, and surface vortices are formed due to wave breaking phenomenon and wave breaking-induced jet. In addition, it was seen that a counterclockwise surface vortex is formed due to a backward wave-breaking phenomenon on the bed discontinuity, and this formed vortex has an interaction with the vortex on the near bed. Because there are many physical mechanisms that affect vortex-vortex interaction, wave-induced dynamics and vortex-induced dynamics were searched apart by implementing a point-vortex model. According to the findings during the experiments, it was determined that the effect of the wave-breaking induced jet is negligible on the surface vortex that has a downward motion, is negligible. Instead of the wave breaking induced jet, mutual interaction and self-advection are two main mechanisms for this situation.

CHAPTER 3

METHODOLOGY

In this chapter, phases of both experimental measurement and data analysis processes of the study are described. In the first part of this chapter, experimental setup is introduced. After that, detailed information is given for experimental measurements. In the third part of the chapter, the signal-denoising process is explained. After this section, the statistical studies and the methods used to find the best signal-denoising method are mentioned. After that, the data analysis process is briefly explained and finally, the methods followed for the analysis of the parameters to be used for dimensionless analysis are explained.

3.1 Experimental Setup

3.1.1 Physical Model

The experiments were conducted at the Coastal and Ocean Engineering Laboratory of the Middle East Technical University (METU) Civil Engineering Department. For the experiments, a wave flume with a length of 26.9 meters, a width of 6 meters, and a depth of 1 meter, where both regular and irregular waves can be tested, was used. A photograph of the wave flume (prior to construction of the cross-section is given in Figure 3.1.

Figure 3.1: Wave flume

In the experiments of this thesis study, a physical model of a head section of a real-life rubble mound breakwater, which is located in the Black Sea region, was used. For the physical model, the head and a relevant portion of the trunk sections were constructed inside the flume. The head and the subsequent trunk section model had a 1/60 Froude-type length scale and had antifer concrete units on its armor layer of the head and trunk armor sections, and tetrapod units at the lee side of the trunk section. Antifer concrete units were placed regularly on the head section and randomly on the trunk section. The face slope of the modeled structure was 1:1.5. A view of this physical model can be seen in Figure 3.2.

A single-block piston-type wave generator was used to generate regular waves during the experiments. At the end of the wave flume, a passive wave absorption system is located to absorb the propagating waves that are generated by the wave generator. In Figure 3.3 and Figure 3.4, the wave generator and passive wave absorption system in the wave flume are shown, respectively.

Figure 3.2: Physical model in the wave flume

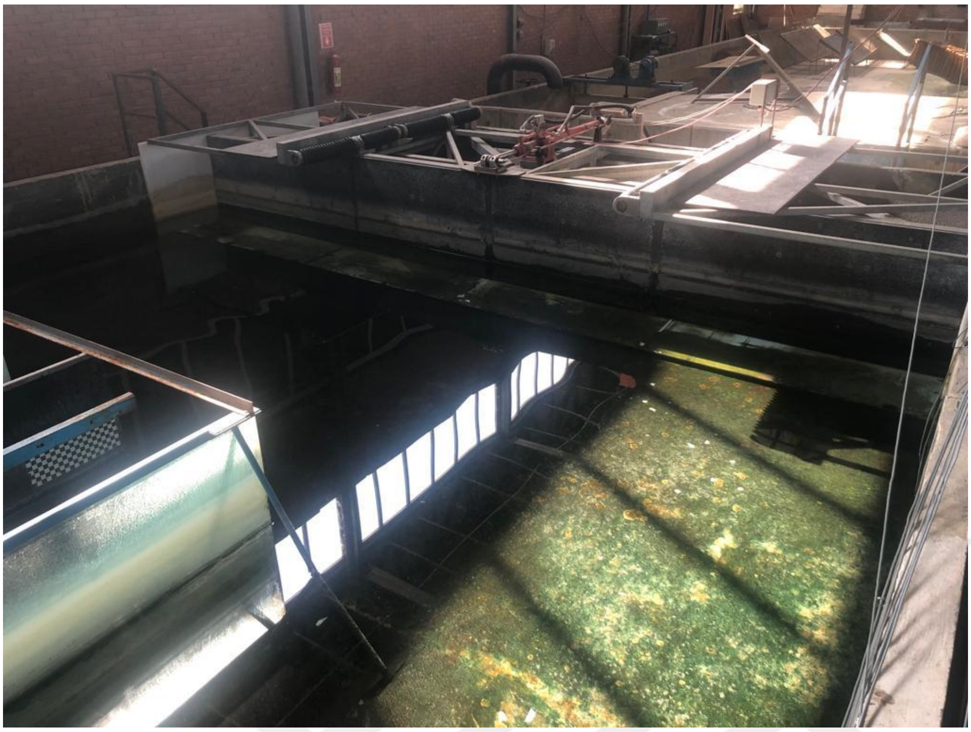

Figure 3.3: Single-Block Piston-Type Wave Generator

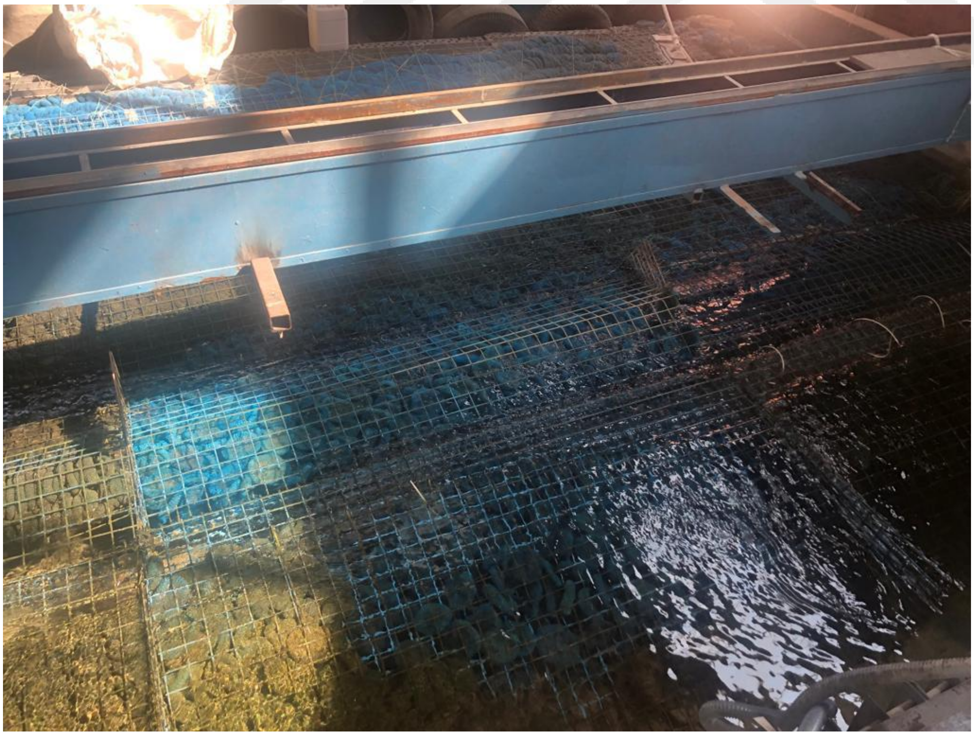

Figure 3.4: Passive Wave Absorption System

In Figure 3.5, plan and cross-section views of the wave basin with the experimental setup is shown. As it can be seen from the figure, both wave gauges were placed 3 m away from the sidewall. First wave gauge was placed 8.46 m, second wave gauge was placed 8.81 m away from the wave generator. 0.2 m in front of the second wave gauge to the physical model, ADV device was located for the undisturbed particle velocity measurements and this point was called as offshore measurement point. A detailed information about ADV measurement points is given in the following section.

The physical model was constructed on a 1:30 slope, which represented the bathymetry of the region of the modeled real-life rubble mound breakwater, and the center of the head section of the physical model was located 3 m away from the sidewall and 14.7 m away from the wave generator.

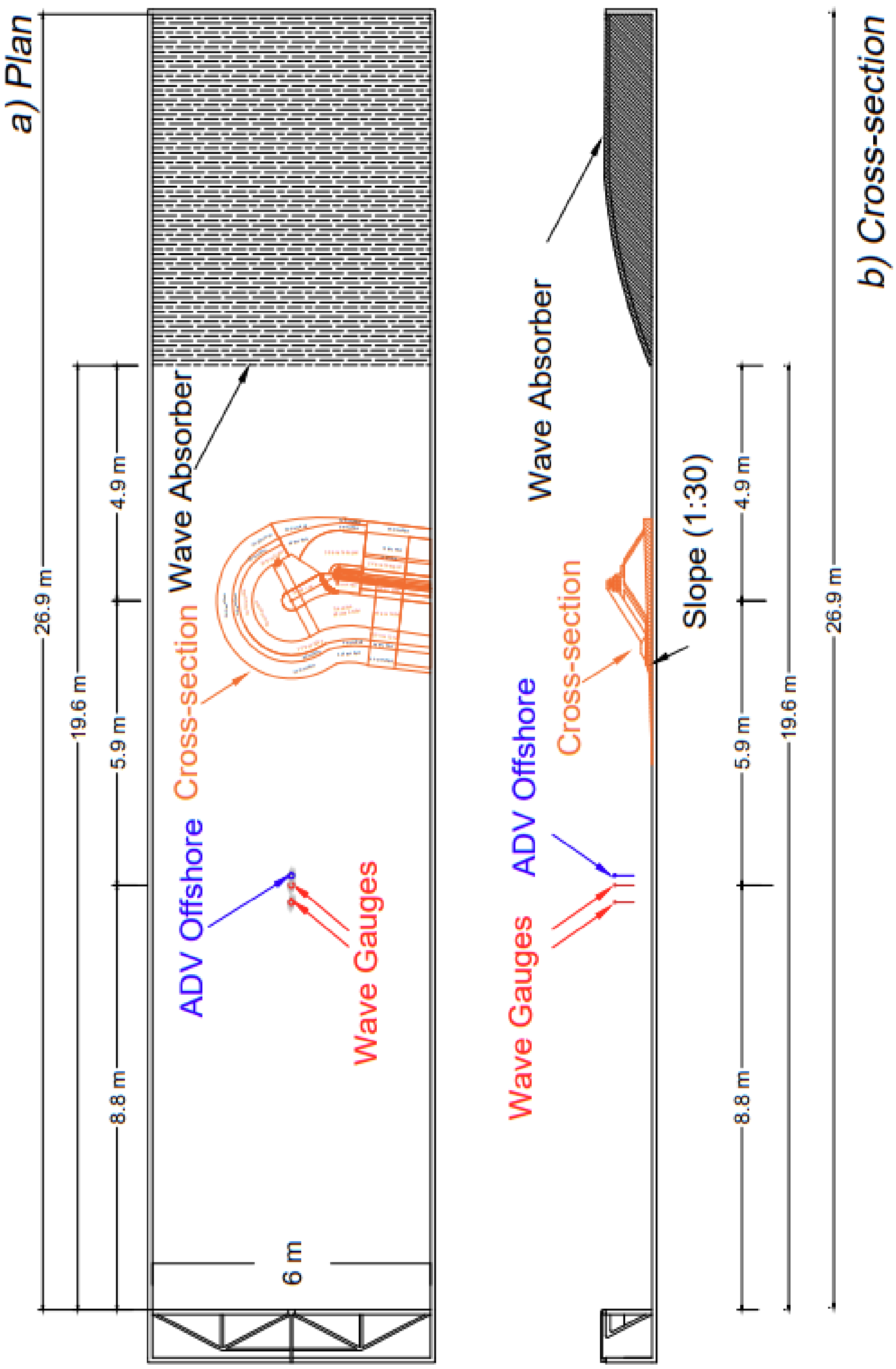

Figure 3.5: Plan and cross-sectional views of the wave flume with the experimental setup

3.1.2 Instrumentation

In the experiments, pressure measurements were performed by a single Kistler Type 601C piezoelectric pressure sensor. This pressure sensor was placed on the lee-side of the head section of the physical model. The location of this sensor was determined according to the video records of the physical model experiments carried out for a consultancy project. These video recordings were taken to observe the damage at the head section under different wave sets. In the present study, the location of the pressure sensor was determined as the area where the most damage occurred in the previous experiments.

To measure the pressure on the surface of armor layer, an antifer block was prepared by using epoxy material with the same sizes as the antifer concrete blocks on the head section's armor layer and the pressure sensor was mounted in this prepared unit. On the armor layer of the head section, antifer concrete blocks which have a 4.8 cm edge length on the top face and a 5.2 cm edge length on the bottom face were used. To insulate the sensor-cable connection and the cable, the epoxy antifer unit is connected to a transparent 1 cm diameter hose and sealed tight. To avoid the bending of the sensor cable, the transparent hose with the cable inside is placed within another larger diameter (1-inch) stiff hose. This hose is placed inside the core of the head section, where one end is at the sensor location and the other end is at the lee side of the trunk section, approximately 10 cm above still water level.

The prepared epoxy antifer unit can be seen in Figure 3.6. This unit was placed in the region where the most damage occurred in the previous experiments, between the other antifer concrete block units. To ensure that the unit remains stable, it is fixed to the other antifers around the unit by hot silicone adhesion.

Figure 3.6: Epoxy and concrete antifer units

Two hoses were used to protect the cable of the pressure sensor from water and kinking. These hoses were intertwined and inserted into the physical model by passing through the core section of the modeled rubble mound breakwater and the cable of the pressure sensor was connected to the pressure sensor by passing through the innermost hose of these intertwined hoses. The other end of the hoses was removed from the trunk section on the lee side of the physical model. The other end of the cable of the pressure sensor was connected to the data acquisition device. A view of the placing process of the hoses inside of the physical model can be seen in Figure 3.7. In Figure 3.8, the connection of the cable of the pressure sensor, which is passed through the pipes, to the end of the sensor, is shown.

Figure 3.7: Placing process of the hoses inside of the physical model

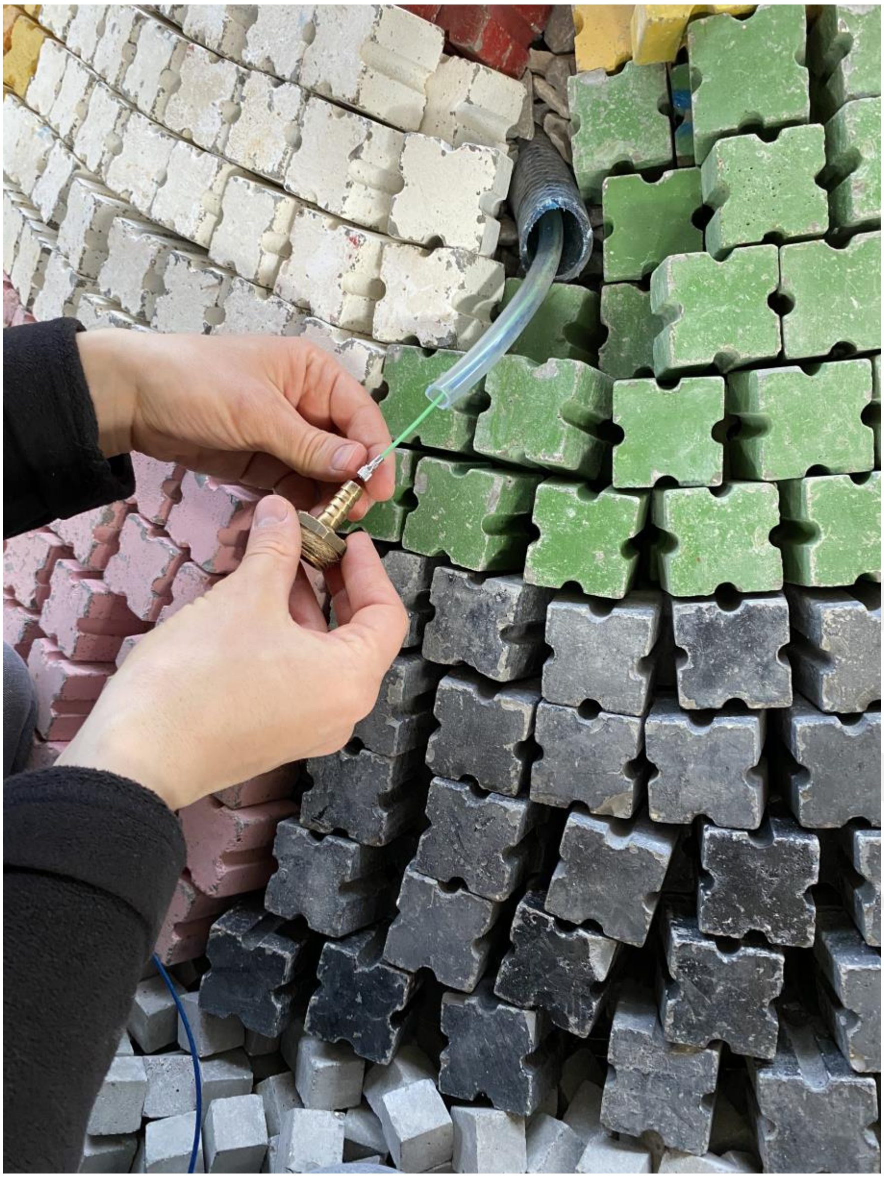

Figure 3.8: Connection of the cable of the pressure sensor and sensor

In Figure 3.9 mounted pressure sensor on the antifer block, which was made from epoxy material and the physical model, is shown.

Figure 3.9: Inserted version of pressure sensor

To measure the water surface elevation, two wave gauges were placed in the channel. Between these two wave gauges, there is 0.35 m and these were located 8.46 m from the front of the wave generator, and 3 m from the front of each sidewall.

ADV measurements were taken at six different points. One of these points is just in front of the wave gauges at the wave basin and the other 5 points are around the head section of the physical model. In Table 3.1, distances of ADV measurement locations to the sidewall and the wave generator when it is at its initial place are given.

Locations of the pressure sensors and ADV measurement points near the head section are shown in Figure 3.10.

Table 3.1: Distances of ADV measurement points to the sidewall and the wave generator

Measurement Point	**Distance to Side Wall (cm)**	**Distance to Wave Generator (cm)**
Offshore	300	901
H1	110	1515
H2	232	1506.3
H3	245	1504.2
H4	245	1519
H5	265.7	1519

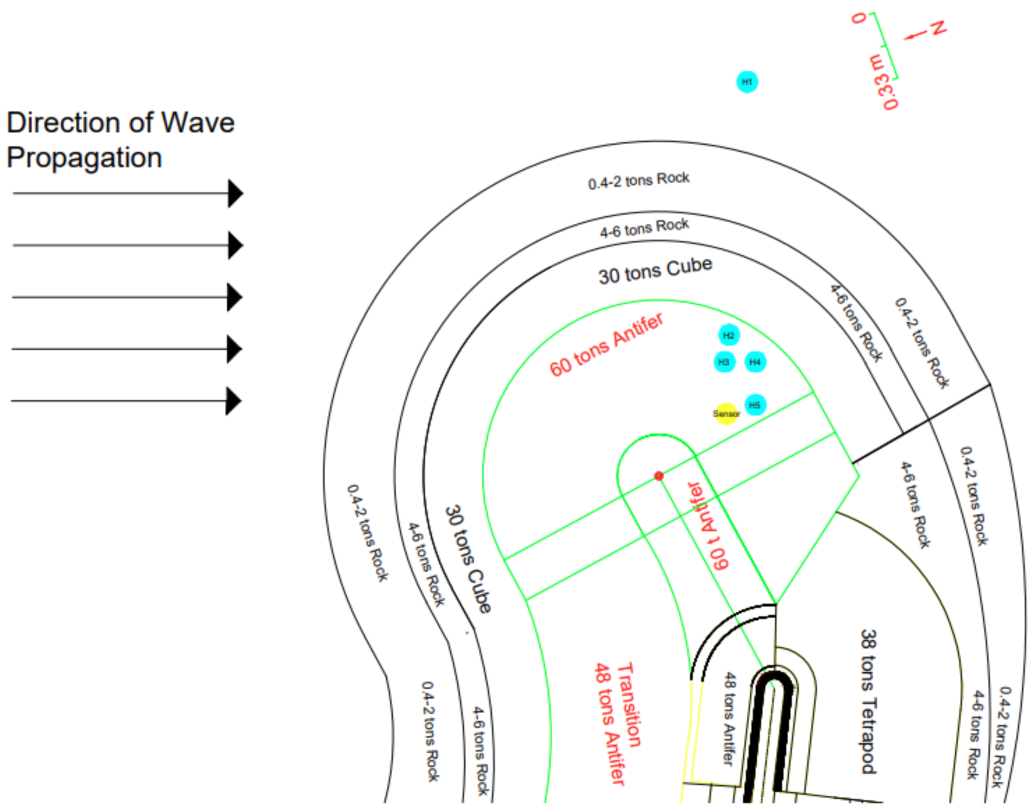

Figure 3.10: Location of the pressure sensor and ADV measurement points near the head section

3.2 Experimental Procedure and Measurements

Experiments were conducted for various wave periods, wave height and water depth conditions. These conditions were determined based on the video recordings and the time series of the water level fluctuations of the irregular wave series of the previous experiments from the instances of the most violent wave breaking and significant rocking or dislocating moments of the armor units. Later, the ranges of these conditions are further extended to increase the coverage and broaden the discussion. In the experiments, a constant wave steepness is considered as H/L = 0.045.

In Table 3.2, the water depths and the wave periods considered in the present study are given.

Table 3.2: Water depths and wave periods used in the experiments

Water Depth (cm)	Wave Period (s)
57	1.7, 1.8, 1.85, 1.9, 2,2.05, 2.1, 2.2, 2.3, 2.4, 2.5
59.5	1.8, 1.85, 1.9, 1.95, 2, 2.05, 2.1
60.4	1.8, 1.85, 1.9, 1.95, 2, 2.05, 2.1, 2.2, 2.4
61.1	1.8, 1.85, 1.9, 1.95, 2, 2.05, 2.1
61.8	1.8, 1.85, 1.9, 1.95, 2, 2.05, 2.1, 2.2, 2.4
62.5	1.7, 1.8, 1.85, 1.9, 1.95, 2, 2.05, 2.1
63	1.7, 1.8, 1.85, 1.9, 1.95, 2, 2.05, 2.1
67	1.5, 1.8, 1.9, 2, 2.1, 2.2, 2.5

Overall, a total 110 tests were performed with 8 different water depths and 13 different wave periods. In each test, 20 regular waves were sent to the physical model through the wave generator. In each wave gauge, the water surface elevation measurements were conducted at 20 Hz sampling frequency. For the pressure measurements, sampling frequencies ranged between 12500 Hz and 62500 Hz. In 91 of 110 tests 62500 Hz sampling frequency was used.

ADV measurements were taken at six different points. One of these points is just 0.2 m in front of the wave gauges at the wave basin and the other 5 points are around the head section of the physical model. These measurements were made only at a water depth of 0.63 m, with regular waves with a period of 1.8 and 1.9 seconds because in these cases, the clearest double-peaked type hydrodynamic loading after wave breaking and vortex formations were seen, which will be discussed in the forthcoming Chapter 4. For each ADV measurement point, measurements were taken with both 25 and 200 Hz sampling frequencies. In Figure 3.11, the ADV device is shown in the wave flume.

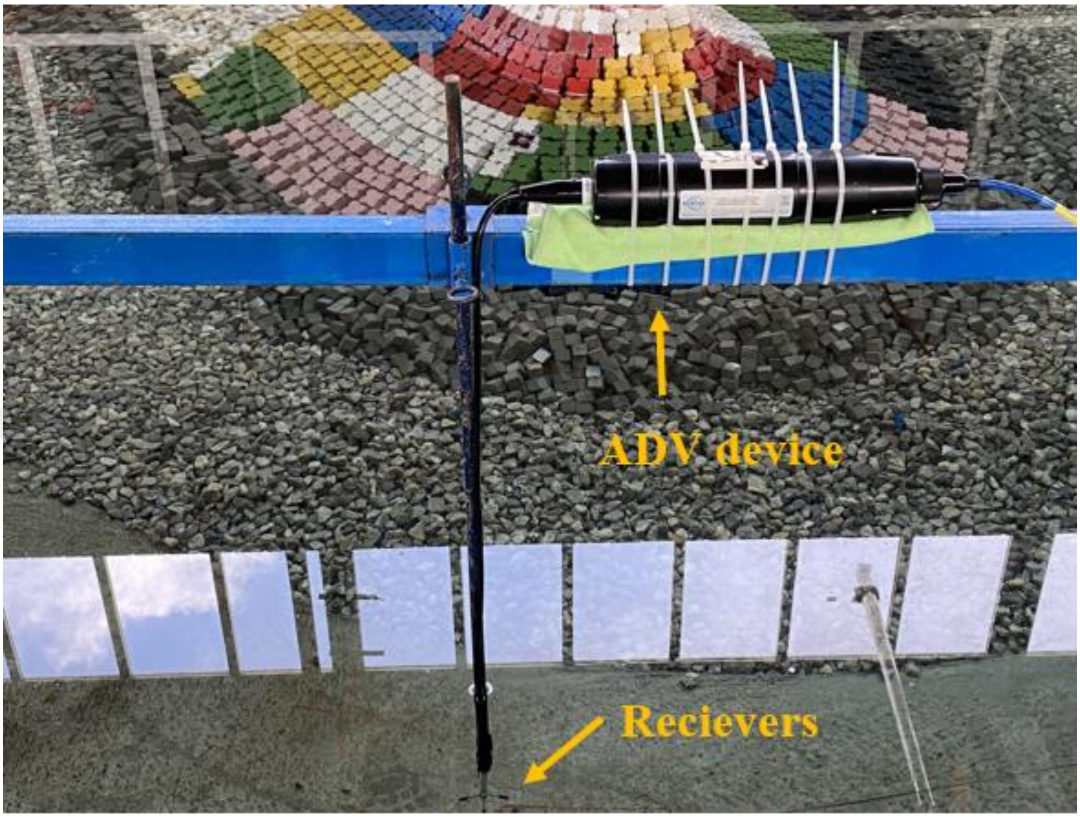

Figure 3.11: ADV device in the wave flume

On every experiment day, the wave basin was filled with water, and at the end of the day, the wave basin was emptied. For water surface elevation measurements by wave gauges, a calibration process was daily conducted. After filling the wave basin, water surface elevation measurements were taken for the calibration process at least two different water levels other than the water level determined for the experiment, and these measurements were taken at a sampling frequency of 20 Hz, as well.

3.3 Signal-Denoising

After the completion of the physical experiment phase, obtained water surface elevation, pressure, and particle velocity measurement data were investigated. It was determined that there is noise in almost all the pressure and velocity measurements at different levels. To get rid of this noise from the obtained measurements, different signal-denoising methods were applied to these measurements to determine the exact measured values from the measurements.

For particle velocity measurements, the Butterworth low-pass filter was applied to all particle velocity data to eliminate the noise. The order of the filter was taken as six and the cut-off frequency of the filter was determined as 2 Hz according to the background noise frequency that was observed in the frequency spectrum of particle velocity measurements. Since the background noise that is observed in the particle velocity measurements is not as high as the background noise observed in the pressure measurements, it was deemed sufficient to use only the Butterworth low-pass filter rather than using multiple signal filtering methods and choosing between them. After the filtering process, the sixth-order Butterworth low-pass filter was found to be suitable for these measurements. In Figure 3.12, an example plot that includes both raw and filtered signals of a particle velocity measurement is given. In this figure, particle velocity values of u-component (wave propagation direction) are shown.

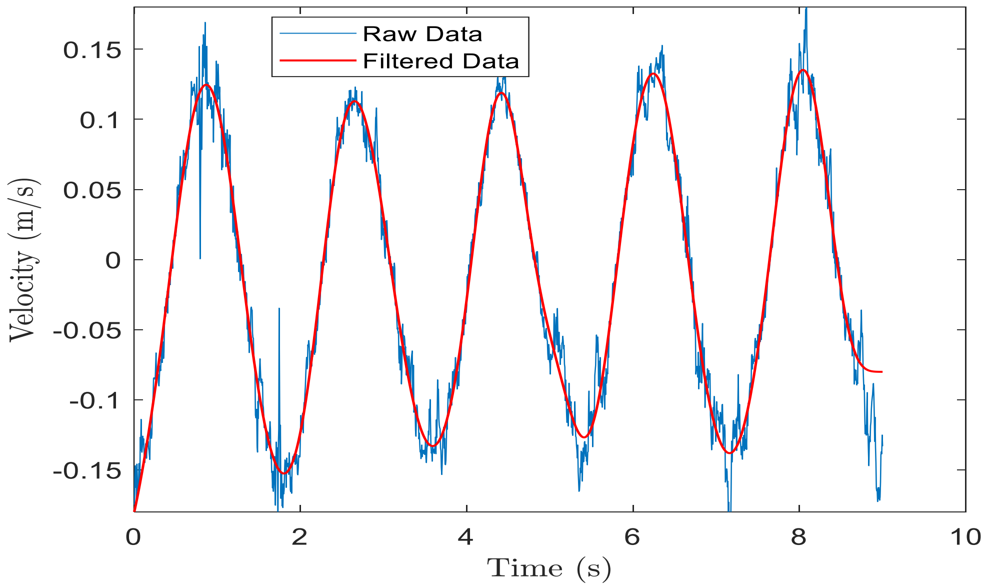

Figure 3.12: Raw and filtered particle velocity signals

For pressure measurements, the finite impulse response (FIR) low-pass filter was applied to all pressure data to eliminate the noise. The order of the filter was taken as 400 and the cut-off frequency of the filter was determined as 45 Hz according to the background noise frequency that was observed in the frequency spectrum of pressure measurements. The order of the filter was determined according to the method that was proposed in the study by Lee et al. (2019). In this study, laboratory experiments were conducted to investigate pressure distribution and flow kinematics of green water loading on a fixed rectangular structure that was placed in a wave flume. In the scope of this study, pressure measurements were taken to observe local loading on the rectangular structure due to green water phenomena. To get rid of the background noise on these pressure measurement data, the finite impulse response (FIR) type low pass filter was applied to the pressure data. The order of the FIR filter was determined to satisfy the below-given conditions (Eq.3.1 and Eq.3.2).

$$R_A(n) = \frac{\int_0^{F_C} S_f(\omega, n)d\omega}{\int_0^{F_C} S_r(\omega)d\omega} \geq 0.9 \tag{3.1}$$

$$R_B(n) = \frac{\int_{F_C}^{\infty} S_f(\omega, n)d\omega}{\int_{F_C}^{\infty} S_r(\omega)d\omega} \leq 0.1 \tag{3.2}$$

In the above-given equations (Eq.3.1 and Eq.3.2) ω represents the frequency, *n*, and F_C represents the order and cut-off frequency of the applied FIR filter, respectively. S_f is given as the spectra of the filtered signal and S_r represents the raw signal in these equations. R_A and R_B are the ratio of the 0^{th} (zeroth) moment of the filtered and raw signals. Equation 1 explains that the ratio of the 0^{th} (zeroth) moment of the filtered and raw signals should be greater than or equal to 0.9 for the lower components of the spectra of both signals than the cut-off frequency. A Equation 2 explains that the ratio of the 0^{th} (zeroth) moment of the filtered and raw signals should be lower than or equal to 0.1 for the higher components of the spectra of both signals than the cut-off frequency. During the determination of the order of the filter, conditions that are given by (Eq.3.1) and (Eq.3.2) were satisfied. In Figure 3.13, an example plot that includes both raw and filtered pressure signals is given.

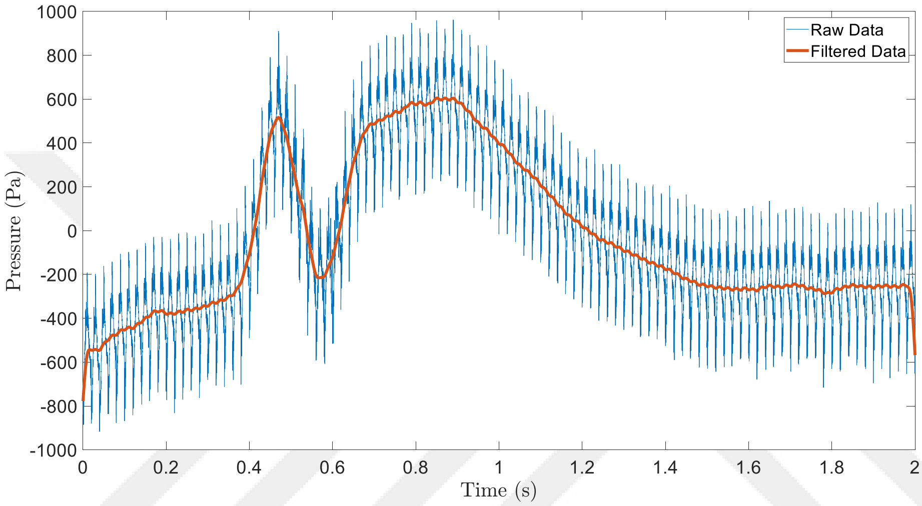

Figure 3.13: Raw and filtered pressure signals

A detailed explanation of the procedure of signal filtering and considered filtering types are also given in Appendix A at the end of this thesis for further information.

To choose the best signal filtering method, eight different statistical analysis methods were applied to the recorded pressure data. A detailed explanation of the procedure of the statistical analysis of the used signal filtering methods and discussions on them are given in Appendix B at the end of this thesis.

3.4 Dimensional Analysis

A dimensional analysis was performed to interpret the results based on physical dimensionless parameters. To apply this analysis, the below-listed dimensional parameters were used.

- Individual wave height (H) – (m)
- Individual wave period (T) – (s)
- Wave Length (L) – (m)
- Maximum pressure values of the first peak of double-peaked hydrodynamic loading type (P_{max}) – (Pa)
- Minimum pressure values of the first peak of double-peaked hydrodynamic loading type (P_{min}) – (Pa)
- Absolute difference of maximum and minimum pressure values of the first peak of double-peaked hydrodynamic loading type (ΔP)
- Gravitational acceleration (g) – (m/s^2)
- Water depth (h) – (m)
- Kinematic viscosity (ν) – (m^2/s)
- Density of water (ρ) - (kg/m^3)
- Bed slope (m)
- Armor layer slope (cotα)
- Crest width (B)
- Circumferential offshore distance in terms of base length of an antifer (ΔX)
- Vertical distance in terms of base length of an antifer (ΔZ)

In Figure 3.14, a definitional sketch is given to present P_{max}, P_{min} and ΔP parameters.

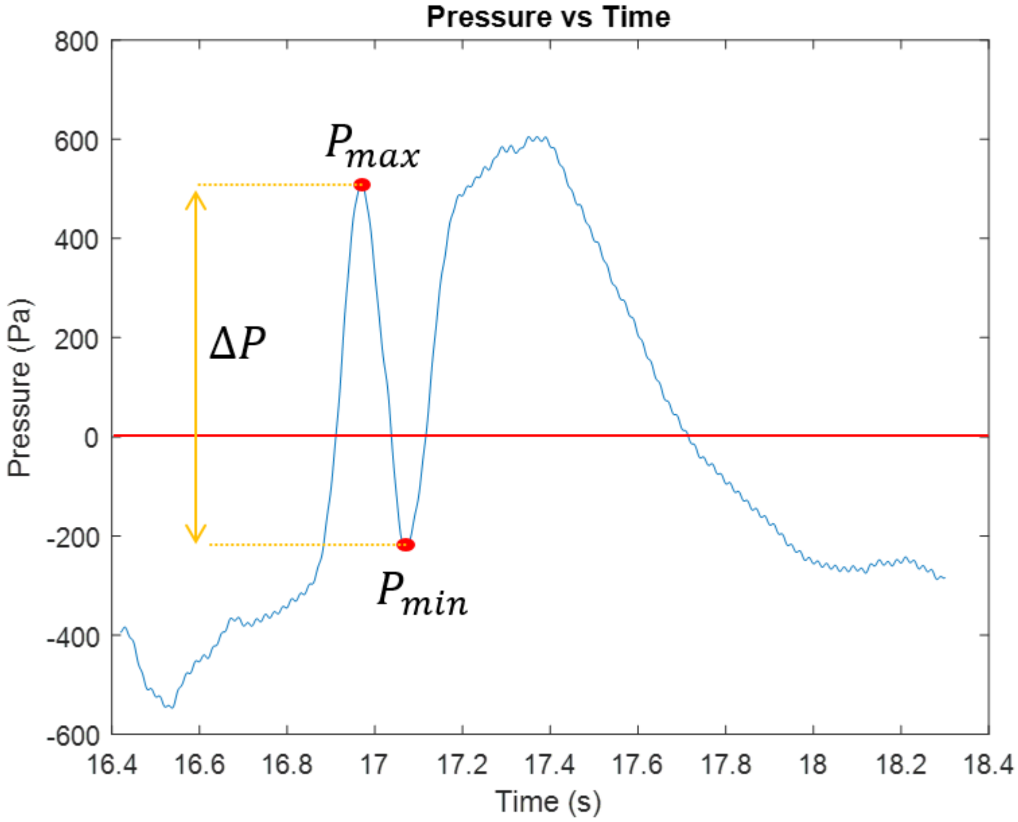

Figure 3.14: Definitional sketch of P_{max}, P_{min} and ΔP

During the analysis of pressure measurements, two types of hydrodynamic loading, which are single-peaked and double-peaked, were observed. In single-peaked type hydrodynamic loading, the breaking wave creates a single peak of pressure, and in the double-peaked type, the breaking wave creates extra maximum and minimum pressure values before the main peak. Thus, above mentioned, P_{max}, P_{min} and ΔP parameters were only determined on the individual waves which created double-peaked type hydrodynamic loading, as it can be seen in Figure 3.12 this is an example for the double-peaked hydrodynamic loading. A detailed explanation of hydrodynamic loading types is given in the next chapter.

In Figure 3.15, a definitional sketch is given to present ΔX and ΔZ parameters.

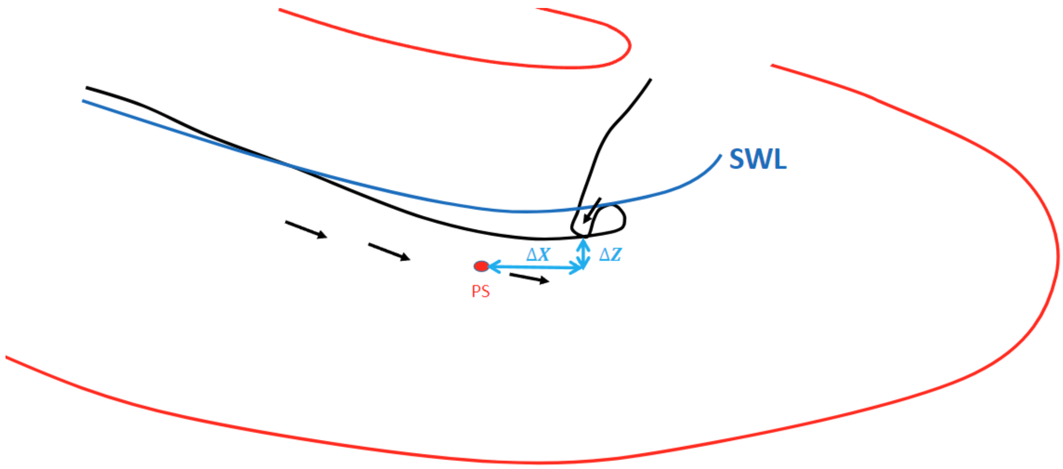

Figure 3.15: Definitional sketch of and ΔX and ΔZ

Below given non-dimensional parameters were derived by using above given parameters for analysis part.

- $\Delta P/\rho g h$
- $\Delta P/\rho g H$
- $P_{min}/\rho g h$
- $P_{min}/\rho g H$
- $\Delta Za/H$
- $\Delta Xa/L$
- $T\sqrt{gH}/h$
- $KC = U_m T/B$

ΔP parameter was non-dimensionalized by dividing ρ, g and h values to observe the effect of water depth values on absolute difference of maximum and minimum pressure values of the first peak of double-peaked type hydrodynamic loading. ΔP parameter was also non-dimensionalized by dividing ρ, g and H values to observe the effect of individual wave height values on absolute difference of maximum and minimum pressure values of the first peak of double-peaked type hydrodynamic loading.

P_{min} parameter was non-dimensionalized by dividing ρ, g, h values to observe the effect of water depth values on minimum pressure values of the first peak of double-peaked type hydrodynamic loading. P_{min} parameter was also non-dimensionalized by dividing ρ, g and H values to observe the effect of individual wave height values on minimum pressure values of the first peak of double-peaked type hydrodynamic loading.

ΔZ and ΔX values are non-dimensional parameters. In order to observe the effect of the wave parameters such as individual wave height and wave period, these non-dimensional parameters are multiplied by *a*, which is the base length of used scaled antifer units, and then these multiplications are divided by *L* and *H*, respectively, according to their axes.

$T\sqrt{gH}/h$ non-dimensional parameter was used to observe the effects of wave parameters which are wave period and wave height, and also water depth on both P_{min} and ΔP parameters. This parameter was introduced in the study of Fredsøe and Sumer (1997), and the original version of this non-dimensional parameter is $T_p\sqrt{gH_s}/h$. In this equation H_s represents the significant wave height and T_p is the peak wave period. This parameter is mentioned as the main governing parameter related to breaker-induced scour, in the above-mentioned study. In the scope of this thesis study, *T* values of individual waves were used instead of T_p and H values of individual waves were used instead of H_s.

$U_m T_p/B$ non-dimensional parameter is known as Keulegan – Carpenter (KC) number. This parameter is mentioned as the main governing parameter related to streaming-induced scour in the study of Fredsøe and Sumer (1997). In this parameter, *B* refers to diameter of the round head of the head section, U_m refers to maximum undisturbed orbital velocity, which is recorded at the sea bottom, and T_p refers to peak wave period. In the scope of this thesis study, *T* values of individual waves were used instead of T_p and crest width value was used instead of diameter of the round head of the head section.

3.5 Data Analysis

As it is mentioned above, each regular wave series used in the experiments were composed of 20 individual waves. Due to the wave reflection, only the first three fully developed individual waves which were not affected by reflection were selected to be analyzed. These waves correspond to the third, fourth, and fifth individual waves. To determine the individual wave height and wave period, the zero-up crossing method was applied to all water surface elevation measurements. The water surface elevation measurements were taken by using two wave gauges and the distance between them was arranged as 0.35 m. For the dimensional analysis, average values of the individual wave height and wave period values from two wave gauges that were placed in the wave flume were taken into consideration. All the data analysis processes such as the application of the zero-up crossing method, data down sampling, signal filtering, statistical analysis of signal filtering, dimensional analysis, and plotting process of the given graphs and results were carried out by using MATLAB R2022a.

In total 110 tests were carried out and 63 of these tests were recorded by camera. For these 63 tests, in other words 189 individual waves, breaking type of the individual waves were determined. 182 of these 189 individual waves, broke in plunging type and, circumferential offshore distance of wave breaking point in terms of base length of an antifer (ΔX) and vertical distance of wave breaking point in terms of base length of an antifer (ΔZ), of these 182 waves were determined for the analysis.

Another important point is that, 50 of 110 pressure measurement results were not used to determine the P_{min} and P_{max} values in the analysis. The reason behind of this situation is that zero-shift occurred in the measurements because the pressure sensor was not continuously submerged under water during wave curling and breaking. This situation occurred especially for the smaller water depth values that are 57 cm, 59.5 cm and 60.4 cm. In the scope of this thesis study, due to used piezoelectric type Kistler pressure sensor was not continuously submerged under the water, both thermal and water level effects caused zero shift on the pressure measurements. Kim et al. (2013) also found a similar result. They conducted an experimental study to determine the differences of pressure sensors (one piezoelectric, one piezosensitive and two integrated circuit piezoelectric sensors). According to their results, piezoelectric and integrated circuit piezoelectric sensors are sensitive to both medium water llevelsand thermal effects. Therefore, for these 50 tests, only ΔP values were taken into consideration. For the remaining 60 test, P_{min}, P_{max} and ΔP values were used in the analysis.

In Figure 3.16 and Figure 3.17, example pressure measurements where zero shift is observed and no zero shift is observed are given, respectively.

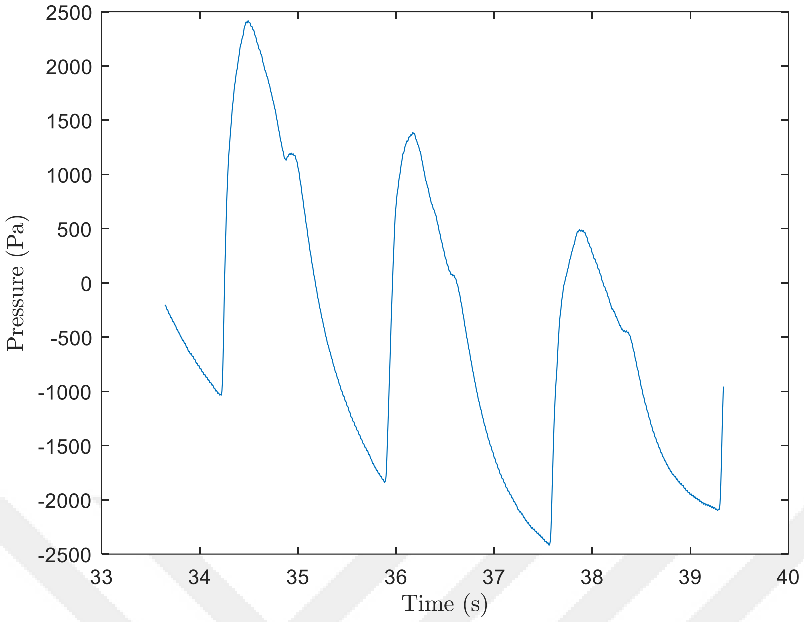

Figure 3.16: Zero shift detected case – 0.57 m water depth, 1.7 s wave period

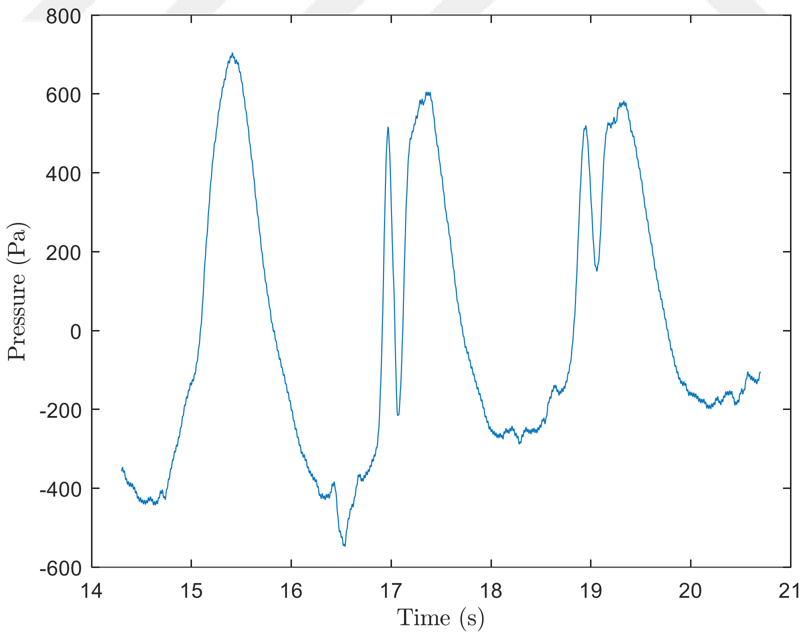

Figure 3.17: Zero shift not detected case – 0.67 m water depth, 1.9 s wave period

CHAPTER 4

RESULTS AND DISCUSSIONS

In this section, the results of the studies that are mentioned in Chapter 3 are given and based on these results, necessary discussions were made. Dimensional analysis process was conducted to observe meaningful relations according to the obtained experimental measurement data as it is mentioned in the previous chapter.

4.1 Wave Conditions

In the scope of this thesis study, total 110 tests were performed with 8 different water depths and 13 different wave periods. Since three individual waves in each of the experiments are used in the analyses to isolate the wave reflection effects as discussed in Chapter 3, in total, 330 individual waves were taken into consideration in this study. 180 of these individual waves were recorded by a camera during the experiments and breaking type of these waves were determined according to the video records. 172 of these individual waves broke in plunging type and five of them broke in surging type and three of them did not broke. Spilling-type wave breaking was not observed in the experiments.

As the first result from the measurements, two main types of pressure distribution were captured in the pressure sensor from all pressure measurement data. These types are named as single peak and double peak pressure distributions. In Figure 4.1, these two types of pressure distributions are shown. In Figure 4.2, corresponding water surface elevation measurement of the pressure measurements that is given in Figure 4.1, is given.

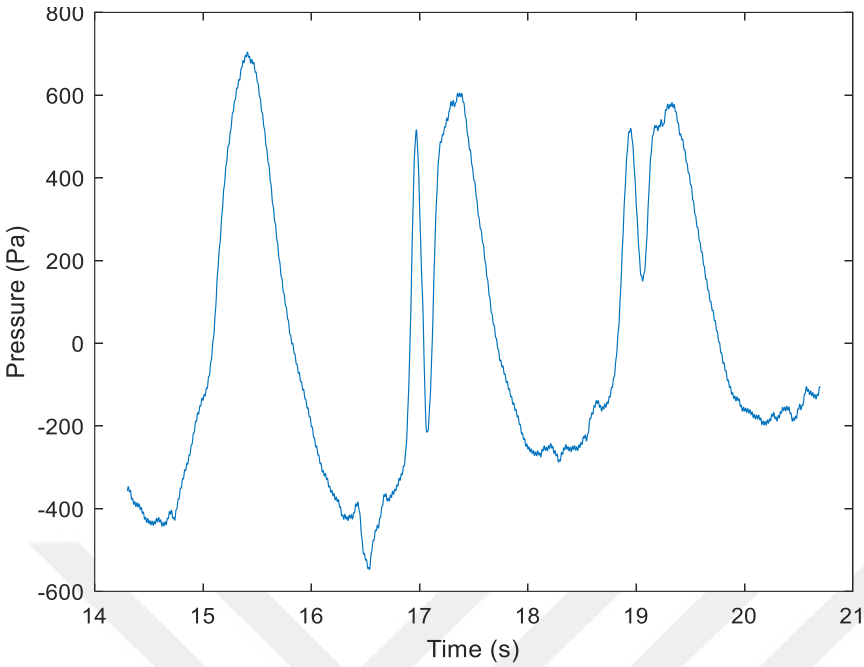

Figure 4.1: Pressure distribution examples (0.67 m water depth, 1.9 s wave period)

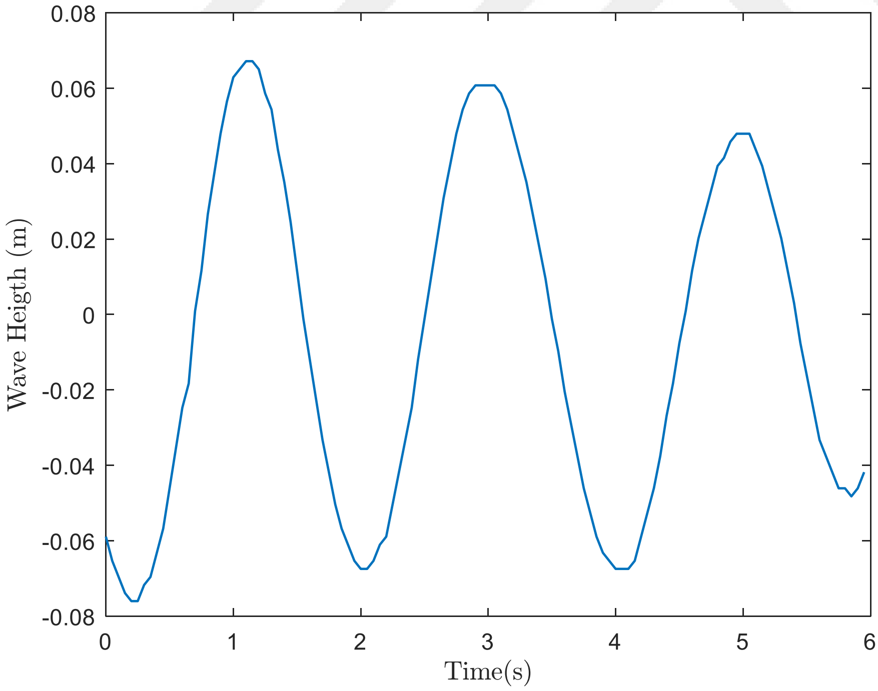

Figure 4.2: Corresponding water surface elevations (0.67 m water depth, 1.9 s wave period)

In Figure 4.1, pressure distributions of three waves in a row can be seen (0.67 cm water depth, 1.9 s wave period test case). The first distribution is an example of the single peak pressure distribution. In this distribution, the passing wave created a single peak in the positive side of the pressure diagram. The second and third pressure distributions are examples for the double peak pressure distribution. Both passing waves created double peaks in the positive side of the pressure diagram. The difference between these two waves is that the minimum point of the first peak of the first wave has a negative value and the first peak of the second wave has a positive value. In order to understand how does these hydrodynamic loading types change under changing wave parameters, a non-dimensional analysis process was carried out.

According to the results, 184 individual waves created double-peaked type hydrodynamic loading and 146 individual waves created single-peaked type hydrodynamic loading.

In Figure 4.3, H vs T is given for the all 330 individual waves.

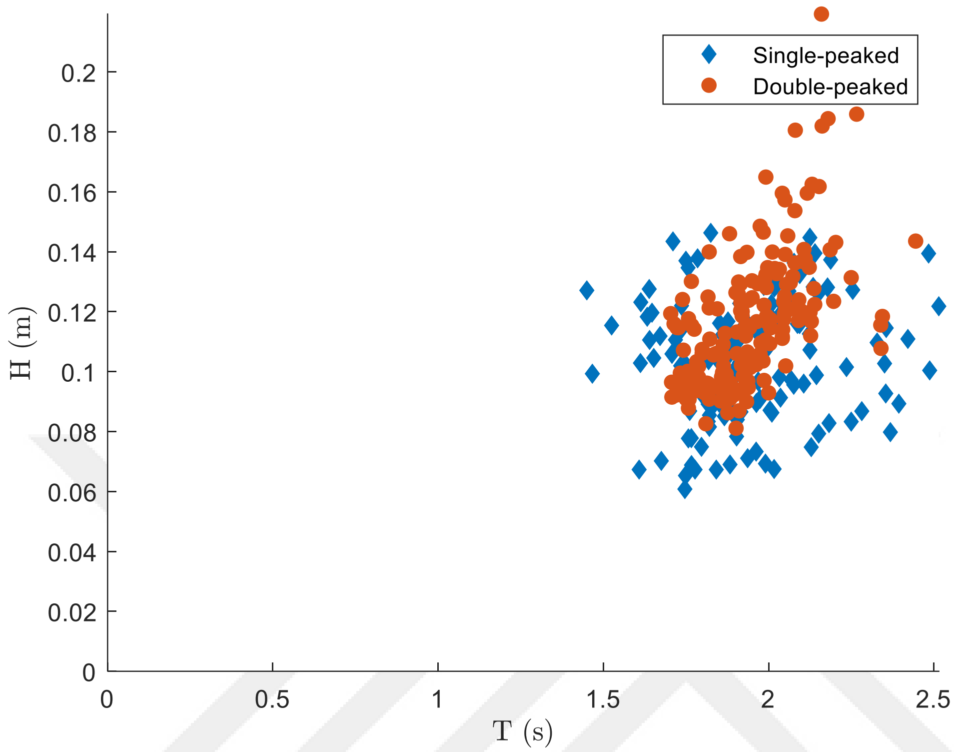

Figure 4.3: T vs H for all recorded individual waves

According to Figure 4.3, if a single outlying data point is ignored, it can be said that individual waves that have single-peaked type hydrodynamic loading on the pressure sensor, have a wider range for individual wave period values than the waves that have double-peaked type hydrodynamic loading on the pressure sensor. Another point is that, the individual wave that have double-peaked type hydrodynamic loading on the pressure sensor have a higher average individual wave height value which is aprroximately 0.12 than the average value of the individual waves that have single-peaked type hydrodynamic loading on the pressure sensor, which is aprroximately 0.10.

In order to present the relation of h/L and H/h non-dimensional parameters, Figure 4.4 is given for the all 330 individual waves.

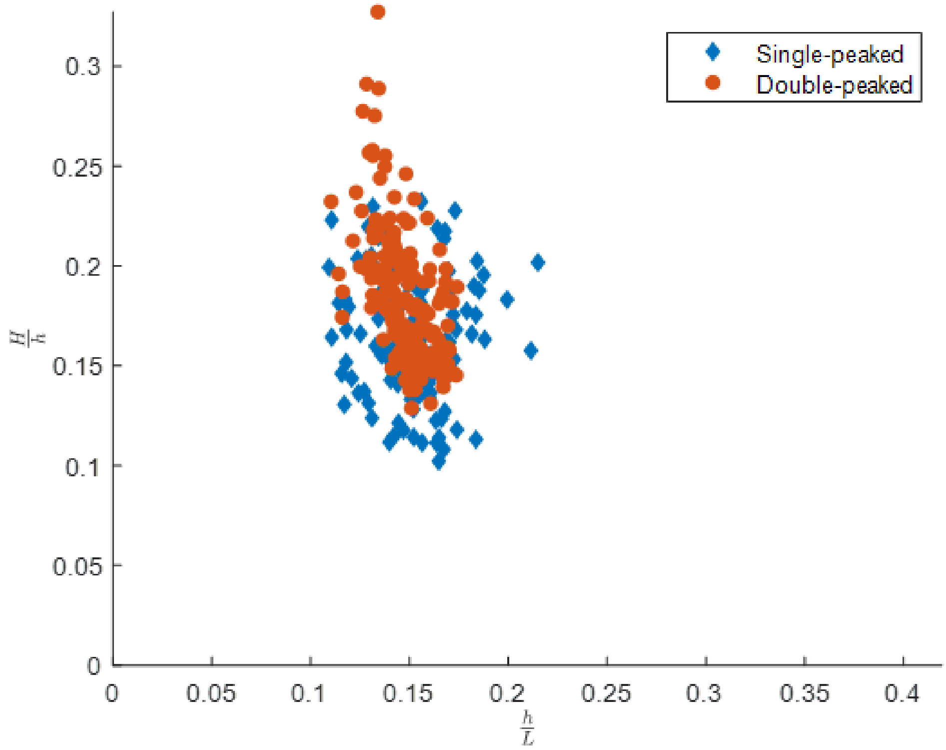

Figure 4.4: h/L vs H/h for all recorded individual waves

According to Figure 4.4, if a single outlying data point is ignored, it can be said that individual waves that have single-peaked type hydrodynamic loading on the pressure sensor, have a wider range for h/L parameter than the waves that have double-peaked type hydrodynamic loading on the pressure sensor. Another point is that, the individual wave that have double-peaked type hydrodynamic loading on the pressure sensor have a higher average H/h value which is aprroximately 0.18 than the average value of H/h that have single-peaked type hydrodynamic loading on the pressure sensor, which is approximately 0.17.

In order to present the relation of h/L and H/h non-dimensional parameters on the the breaking type, Figure 4.5 is given for the 180 individual waves that were recorded by camera during the experiments.

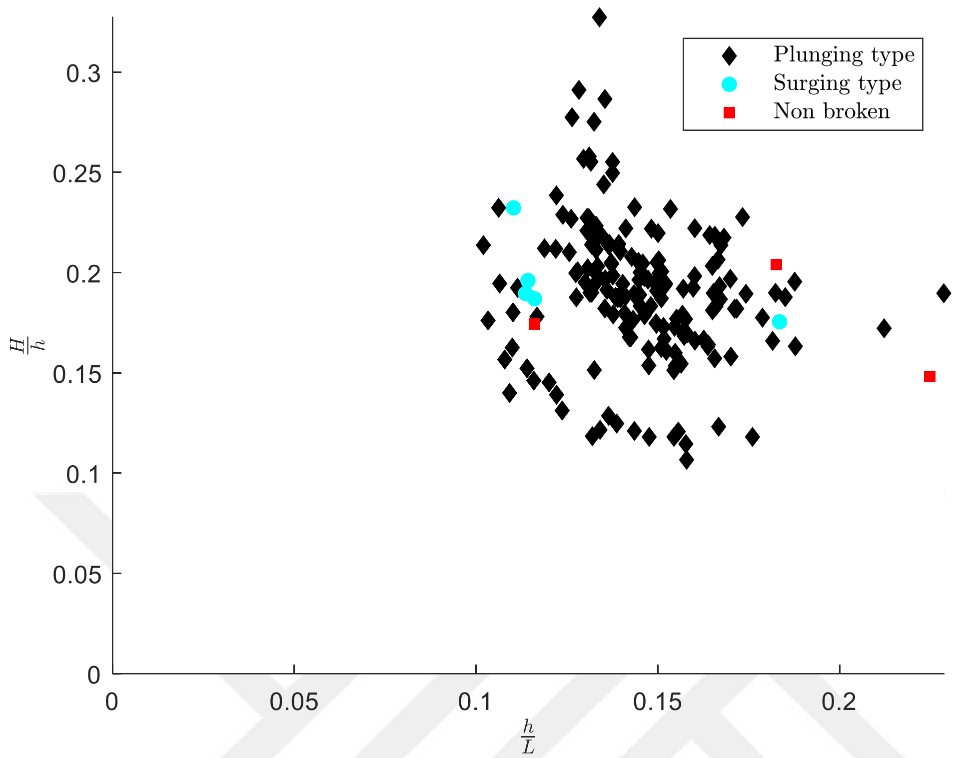

Figure 4.5: h/L vs H/h for breaking types of 180 individual waves

According to Figure 4.5, except one, four of the individual waves that broken in surging type. h/L values of these four individual waves are almost the same, even H/h values of three of these waves almost same, as well. In Figure 4.6 and Figure 4.7, examples are given for surging and plunging types of wave breaking, respectively, from the video records of the experiments.

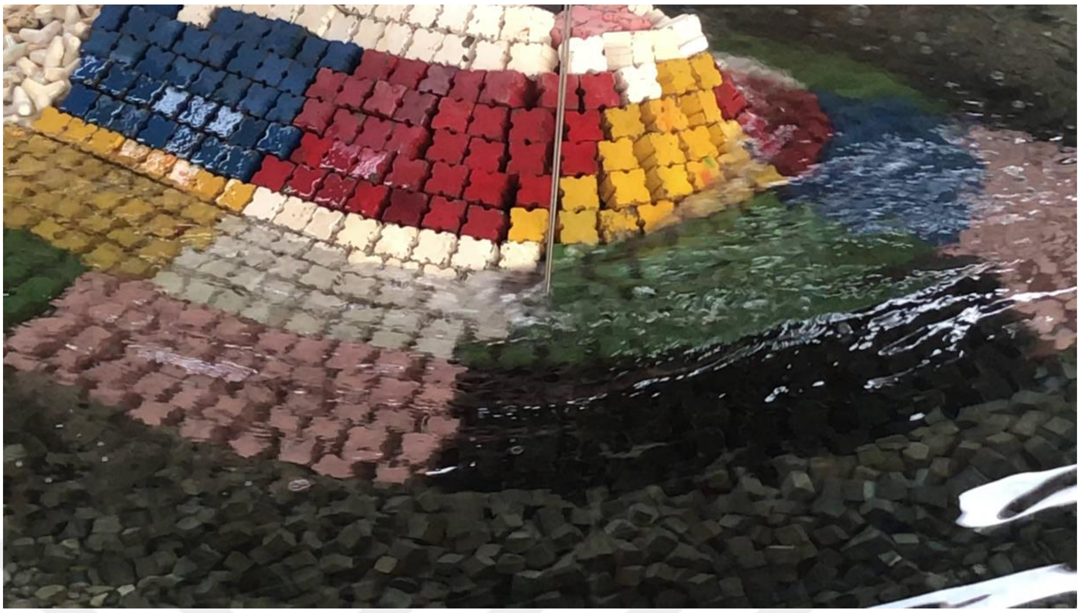

Figure 4.6: Surging type wave breaking (61.8 cm water depth, 2.4 s wave period)

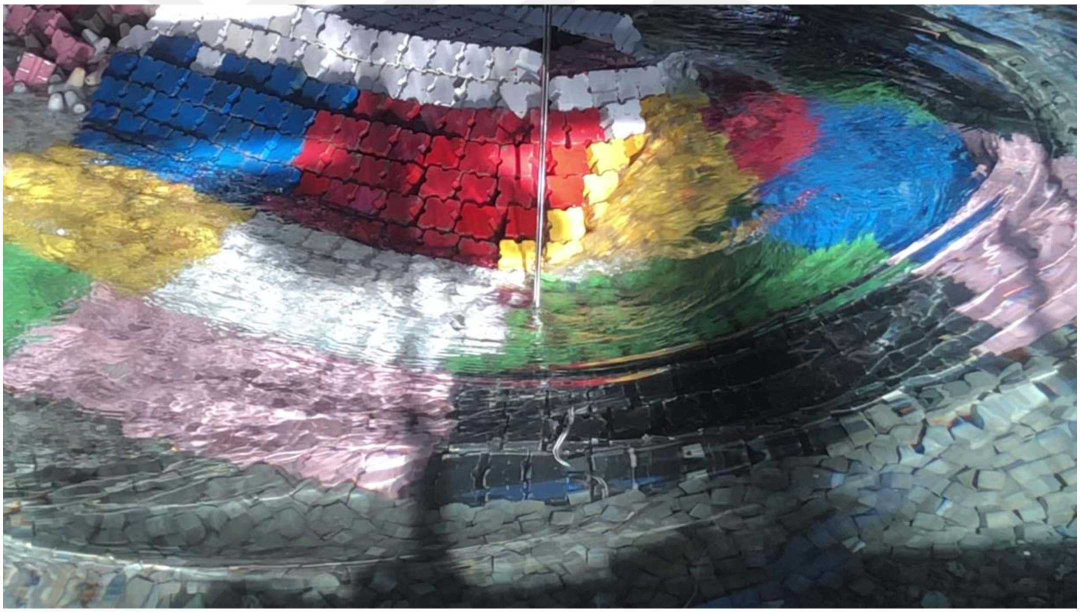

Figure 4.7: Plunging type wave breaking (67.0 cm water depth, 1.9 s wave period)

For non-broken waves, there is a wide range of h/L values and this value is closer to the range of individual waves that broken in plunging type. H/h range of non-broken waves is relatively smaller to the h/L range. However, there is there is significant difference in the number of occurrences of the observed breaking types.

There are only five individual waves with surging type of breaking and three non-broken waves. With such a small amount of data compared to waves with plunging type breaking, it would not be meaningful to observe a relation with breaking types and h/L and H/h parameters. Nevertheless, it should be noted that non-broken waves created single-peaked type hydrodynamic loading on the pressure sensor while the these wave passed over the sensor.

4.2 Particle Velocity Measurements

In this part of this chapter, results from The ADV measurements and discussions on these results are given. As it is mentioned in Chapter 3, particle velocity measurements were carried out at six different locations in the wave flume. One of these locations was just in front of the wave gauges and five of these were near to the head section. Detailed location information can be found in Table 3.1 and Figure 3.10. These measurements were taken by using the ADV device. Measurements were carried out only for 0.63 m water depth value. 1.8 s and 1.9 s wave period values were applied for these tests because in these cases, the clearest double-peaked type hydrodynamic loading after wave breaking and vortex formations were seen. The sampling frequency of measurements was determined as 200 Hz.

Due to the background noise, particle velocity measurements were also filtered like pressure measurement data. Sixth order Butterworth low-pass filter was applied to the data with 2 Hz cut-off frequency, which was determined according to the frequency spectrum. Used ADV device has three receiver arms and it can measure the particle velocity component on both horizontal and vertical directions. During the analysis of the ADV measurements, particle velocities were used on the direction of propagating wave. To make an inference from the results, particle velocity measurement results of three waves, which were also used for the pressure measurements, were taken into consideration. The results are given below in Table 4.1, for all measurement points for both 1.8 s and 19.s wave periods cases. These results are the average values of the analyzed three waves for all measurement points.

According to the results, it is seen that velocities significantly increase closer to the lee-side of the head section up to more than three times the undisturbed values for both1.8 s and 1.9 s wave period cases. and up to three times the undisturbed values for 1.9 s wave period case.

Table 4.1: Measured mean maximum orbital velocities for all measurement points

Measurement Point	$U_m\ (m/s)$ – (1.8 s)	$U_m\ (m/s)$ – (1.9 s)
OS	0.11	0.10
H1	0.14	0.15
H2	0.23	0.24
H3	0.28	0.29
H4	0.36	0.43
H5	0.37	0.36

4.3 Pressure Measurements

From the video records and pressure measurements, formation process of double peak type hydrodynamic loading with a passing wave was tried to be understood. This process is also important to observe the effects of formation of local vortices near to the pressure sensor on the hydrodynamic loading. For this purpose, one of the studied pressure measurements was selected and this study was conducted on this measurement. As it is mentioned in Chapter 3, due to the wave reflection phenomenon, only three individual waves which were not affected by reflection were selected to be analyzed and two of these waves are shown in Figure 4.8. As it can be seen in this figure, first wave has a double-peaked type hydrodynamic loading after wave breaking. Second wave has also a double-peaked type hydrodynamic loading but the minimum pressure value of the first peak has a positive rather than a negative values as second wave has. These waves were selected to examine the wave breaking process to understand the formation of a double peak type hydrodynamic loading after wave breaking. Selected points were found in the video record and a sequence of sketches was drawn to introduce the procedure of wave breaking and this process was related with the hydrodynamic loading. Locally formed vortices are also shown in these sketches. This sequence of sketches is given in Figure 4.9, Figure 4.10, Figure 4.11 and Figure 4.12. Definitions of each step are also given below. From these sketches and below-given information about the processes, the difference between the two individual wave that have double-peaked type hydrodynamic loading with different types of minimum pressure value in their first peak.

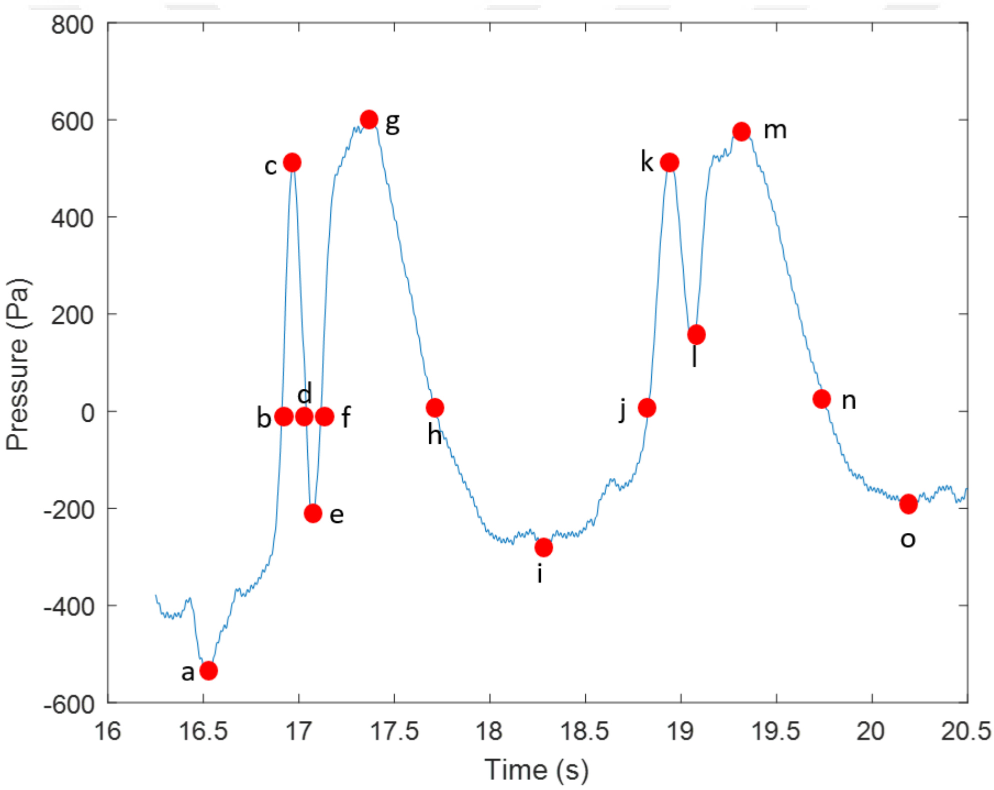

Figure 4.8: Studied hydrodynamic type and studied points

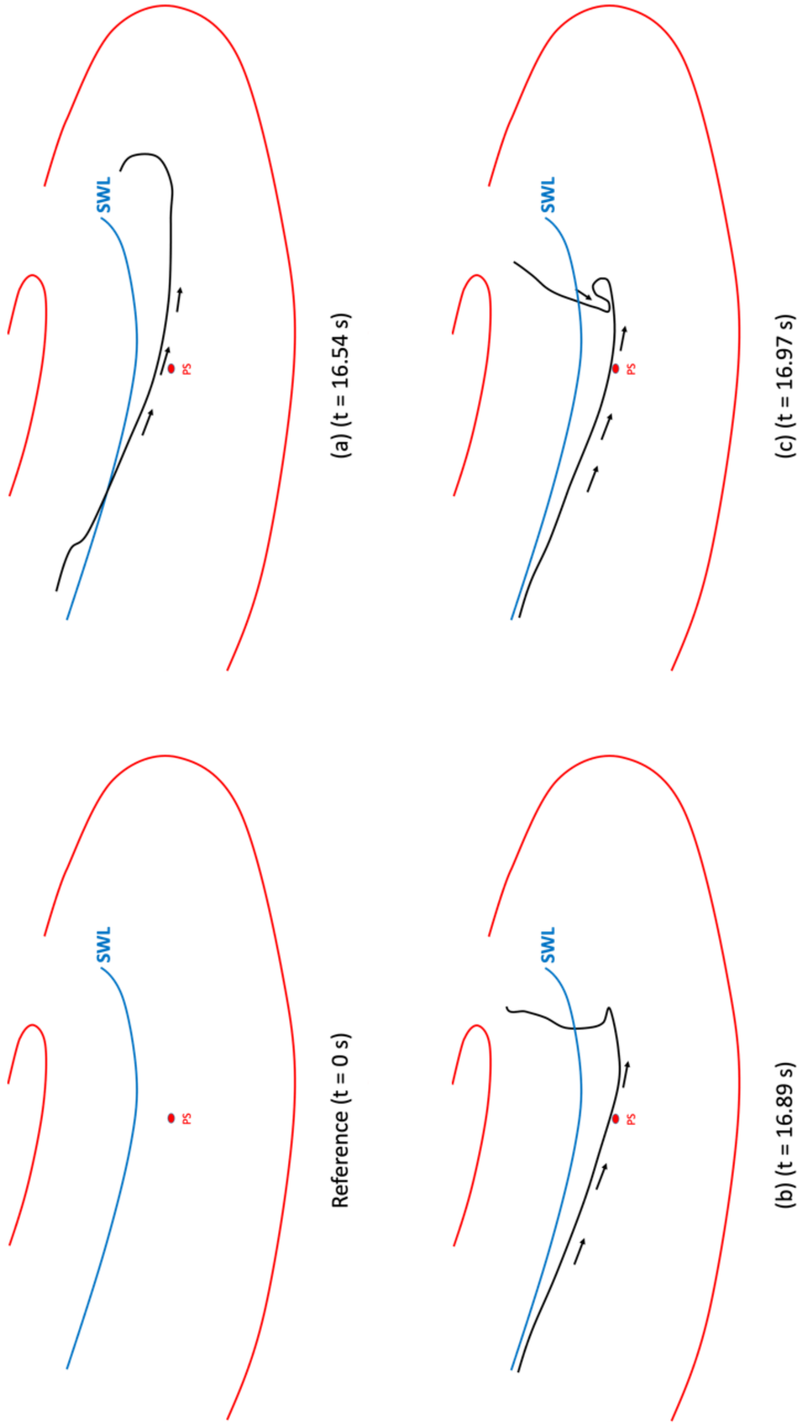

Figure 4.9: Sketches for reference, a, b and c frames

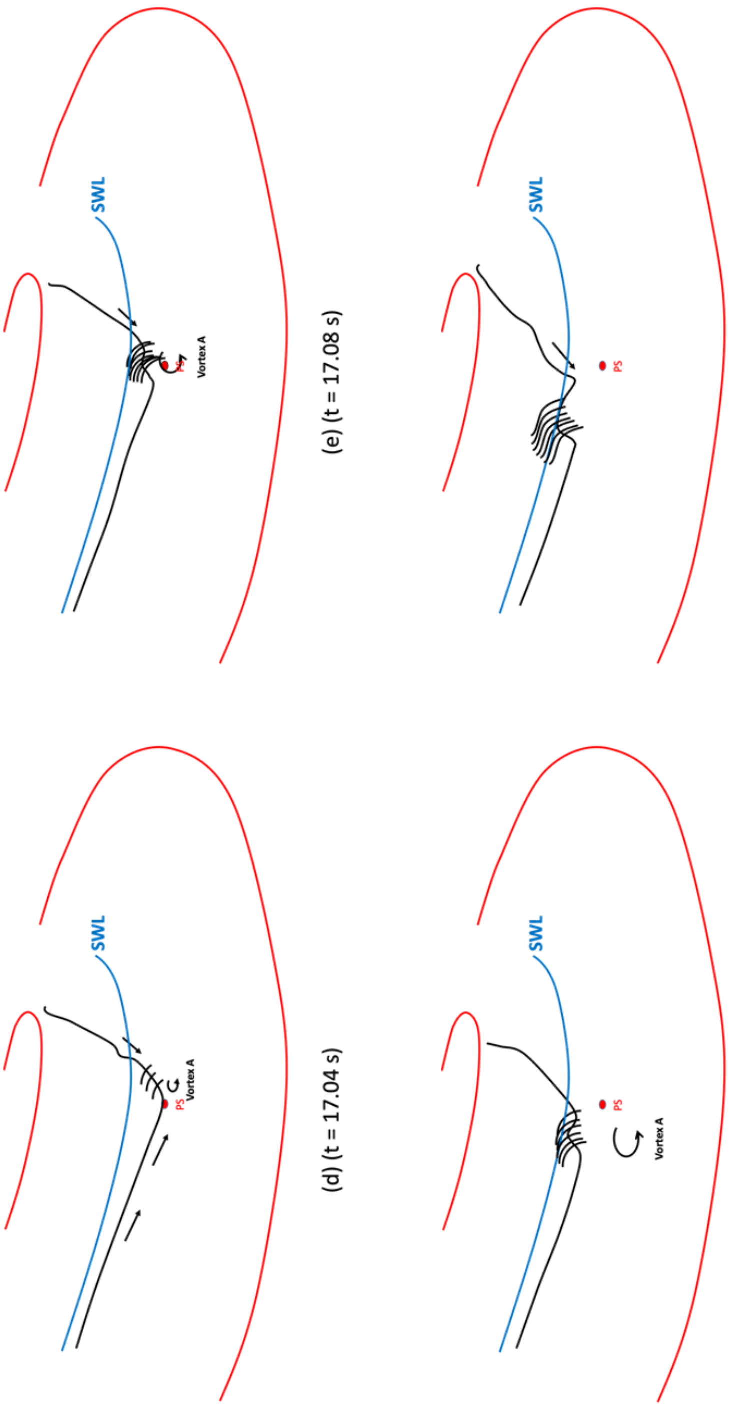

Figure 4.10: Sketches for d, e, f and g frames

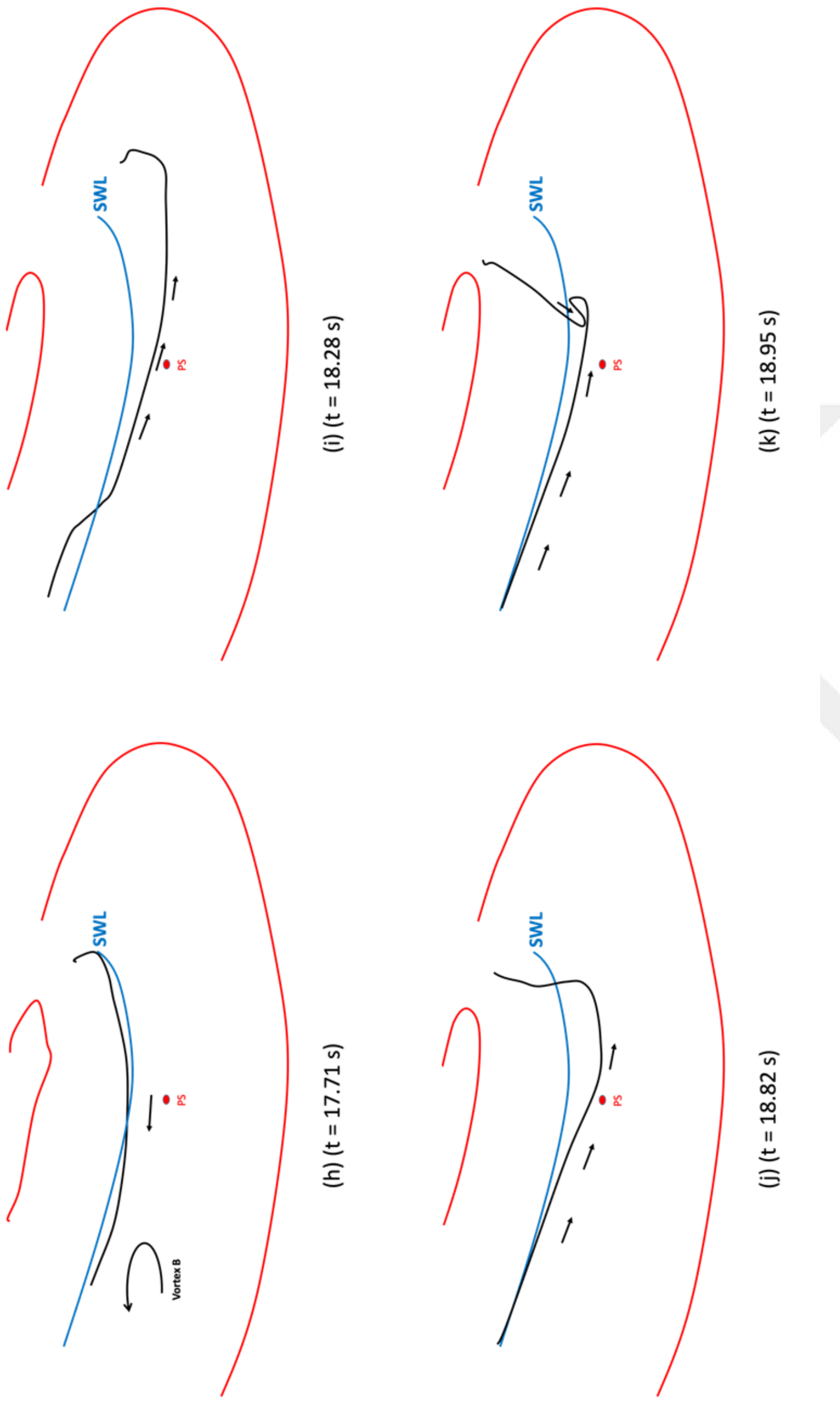

Figure 4.11: Sketches for h, i, j and k frames

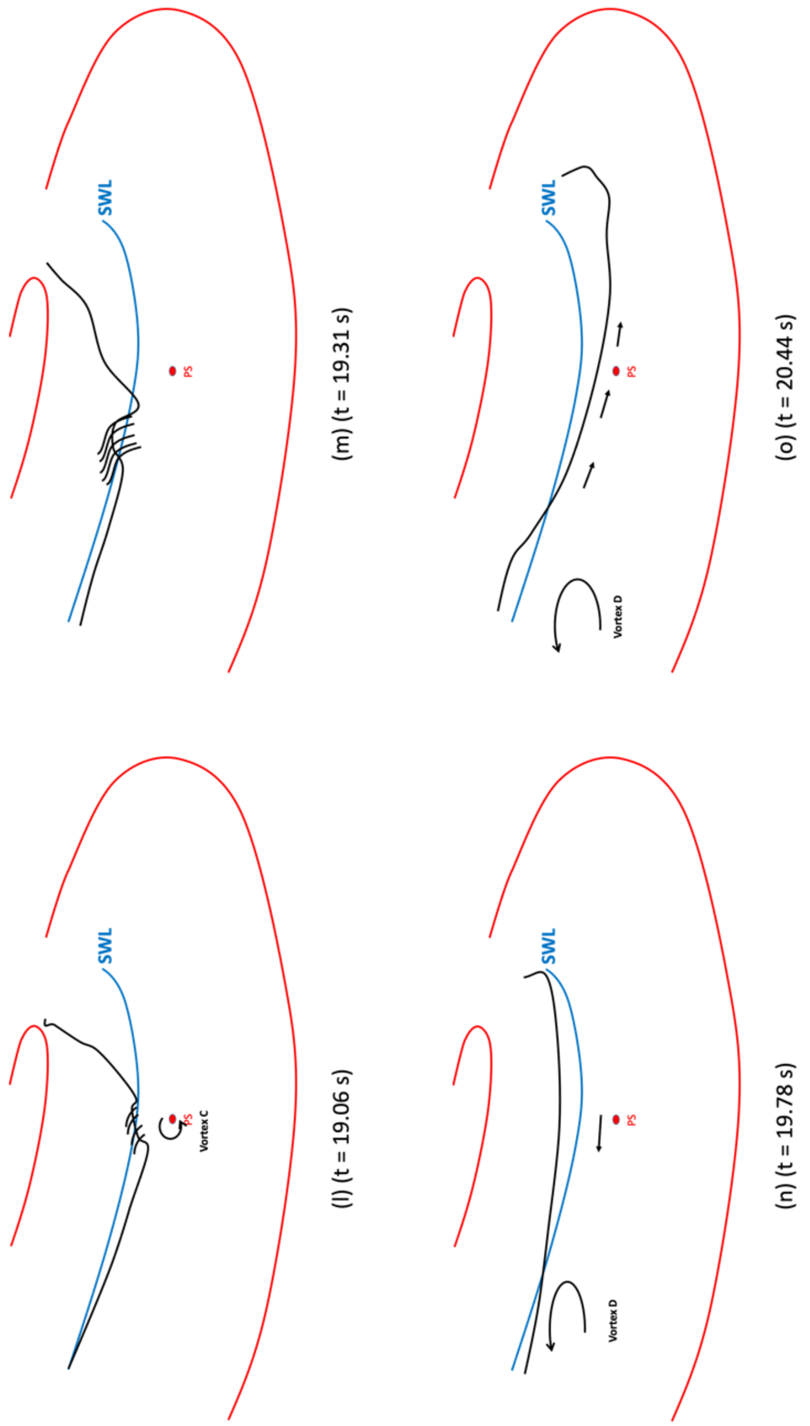

Figure 4.12: Sketches for l, m, n and o frames

In frame (a) (t = 16.54 s), offshore-directed flow caused by rundown process after wave breaking of previous individual wave is shown. At this moment, minimum pressure value of the hydrodynamic loading is observed for the previous individual passing wave.

In frame (b) (t = 16.89 s), over-curling process step is shown and this step is seen when the velocity of the crest of the wave is more than the velocity of the trough of the wave.

In frame (c) (t = 16.97 s), plunger shape can be seen. This shape is formed just before the wave breaking process. At this moment, maximum value of the first peak is seen.

In frame (d) (t = 17.04 s), beginning of the wave breaking process is shown. At this moment, jet impingement process occurs and a vortex (Vortex A) is formed at just right side of the pressure sensor.

In frame (e) (t = 17.08 s), the ongoing process of wave breaking is shown. At this moment, minimum pressure value is observed for the first peak of the hydrodynamic loading. At the same time, formed vortex (Vortex A) during jet impingement moment, which is shown in frame (d), is seen on the pressure sensor location as more grown up.

In frame (f) (t = 17.13 s), the ongoing process of wave breaking is shown. At this moment, formed vortex (Vortex A) is vanished and pressure value is increasing again with the vanishing vortex and coming crest level of the breaking wave.

In frame (g) (t = 17.37 s), maximum pressure value of the second peak is observed. At this moment, crest of the breaking wave is passing through the top level of the pressure sensor.

In frame (h) (t = 17.71 s), the end the wave breaking process (breaking wave is totally converted to foam) is shown. At this moment, a following vortex (Vortex B) is formed after the pressure sensor.

In frame (i) (t = 18.28 s), offshore-directed flow caused by rundown process after wave breaking of previous individual wave is shown. At this moment, minimum pressure value of the hydrodynamic loading is observed for the first wave.

In frame (j) (t = 18.82 s), over-curling process step is shown for the second wave.

In frame (k) (t = 18.95 s), plunger shape of the second wave can be seen. This shape is formed just before the wave breaking process. At this moment, maximum value of the first peak is seen.

In frame (l) (t = 19.06 s), the ongoing process of breaking of the second wave is shown. At this moment, minimum pressure value is observed for the first peak of the hydrodynamic loading. At the same time, formed vortex (Vortex C) during jet impingement moment is seen at immediately after passing the pressure sensor. Due to this situation, impact of the formed vortex (Vortex C) is less than Vortex A, so the minimum pressure value of the first peak has appositive values rather than a negative value.

In frame (m) (t = 19.31 s), maximum pressure value of the second peak is observed. At this moment, crest of the breaking wave is passing through the top level of the pressure sensor.

In frame (n) (t = 19.78 s), the end the wave breaking process (breaking wave is totally converted to foam) is shown. At this moment, a following vortex (Vortex D) is formed after the pressure sensor.

In frame (o) (t = 20.44 s), offshore-directed flow caused by rundown process after wave breaking of second wave is shown. At this moment, minimum pressure value of the hydrodynamic loading is observed for the second wave.

In order to observe the relation between $P_{min}/\rho gh$ - $P_{min}/\rho gH$ parameters and ΔX-ΔZ parameters, seperately, below given figures (Figure 4.13, 4.14, 4.15 and 4.16) are plotted.

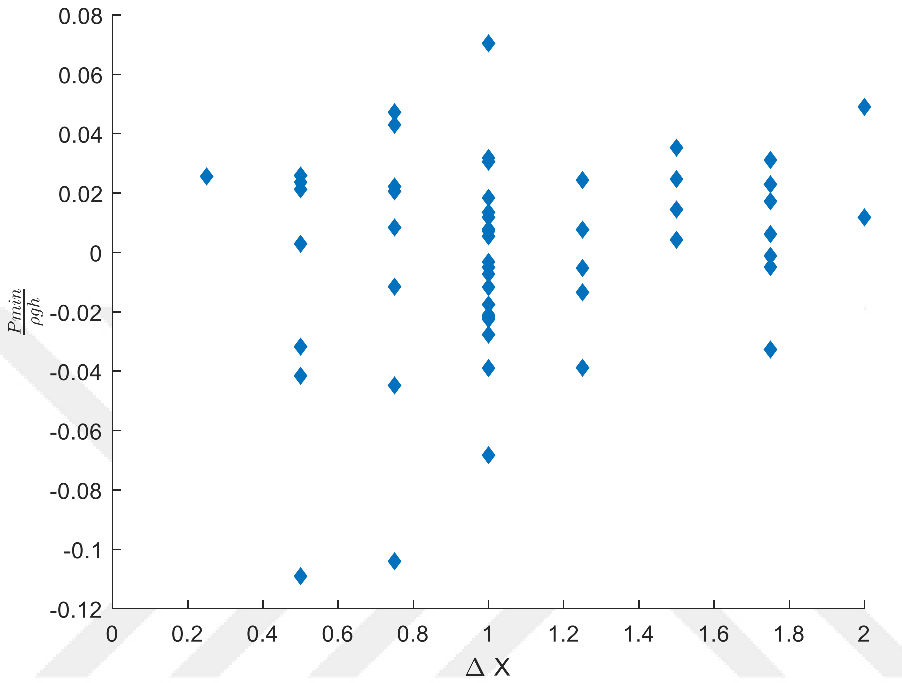

Figure 4.13: ΔX vs $P_{min}/\rho gh$ for individual waves with double-peaked hydrodynamic loading

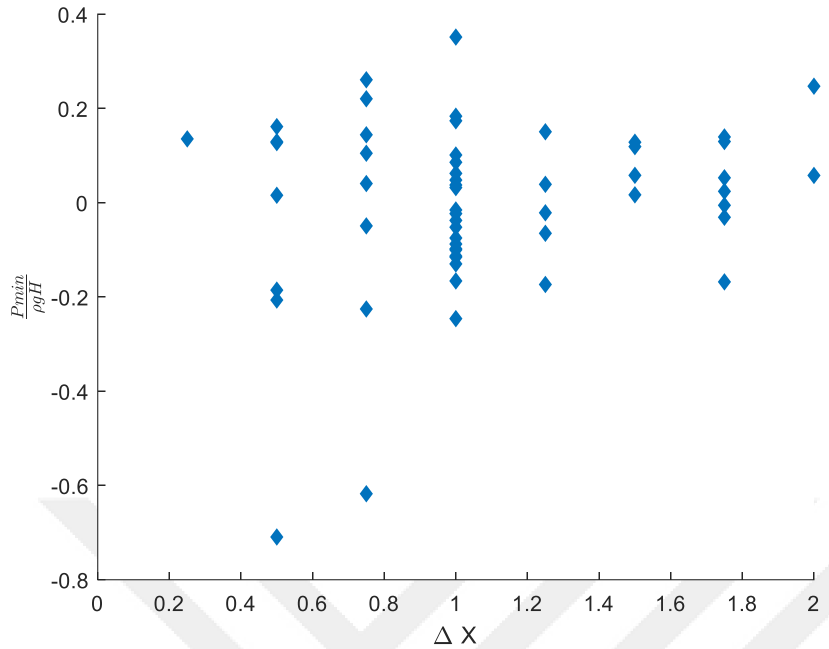

Figure 4.14: ΔX vs $P_{min}/\rho g H$ for individual waves with double-peaked hydrodynamic loading

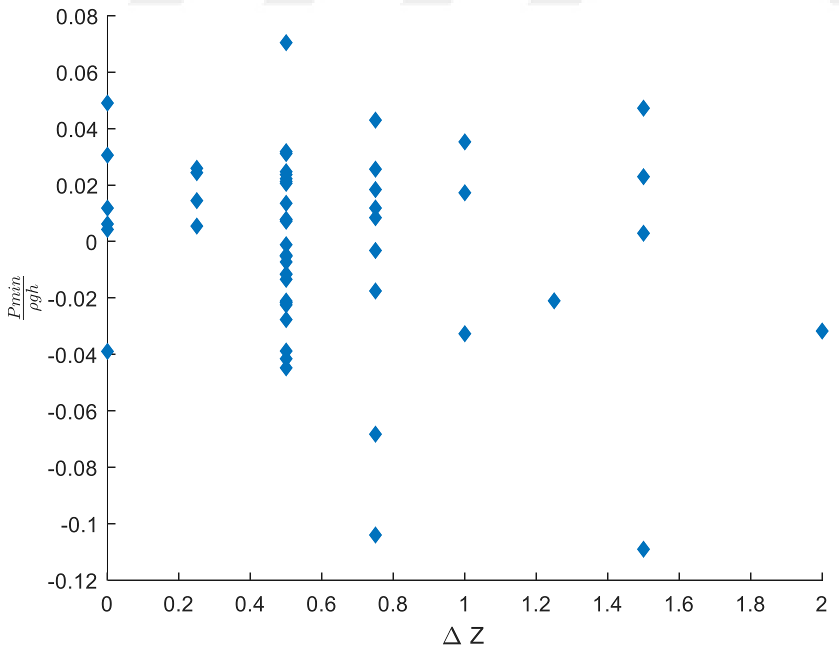

Figure 4.15: ΔZ vs $P_{min}/\rho g h$ for individual waves with double-peaked hydrodynamic loading

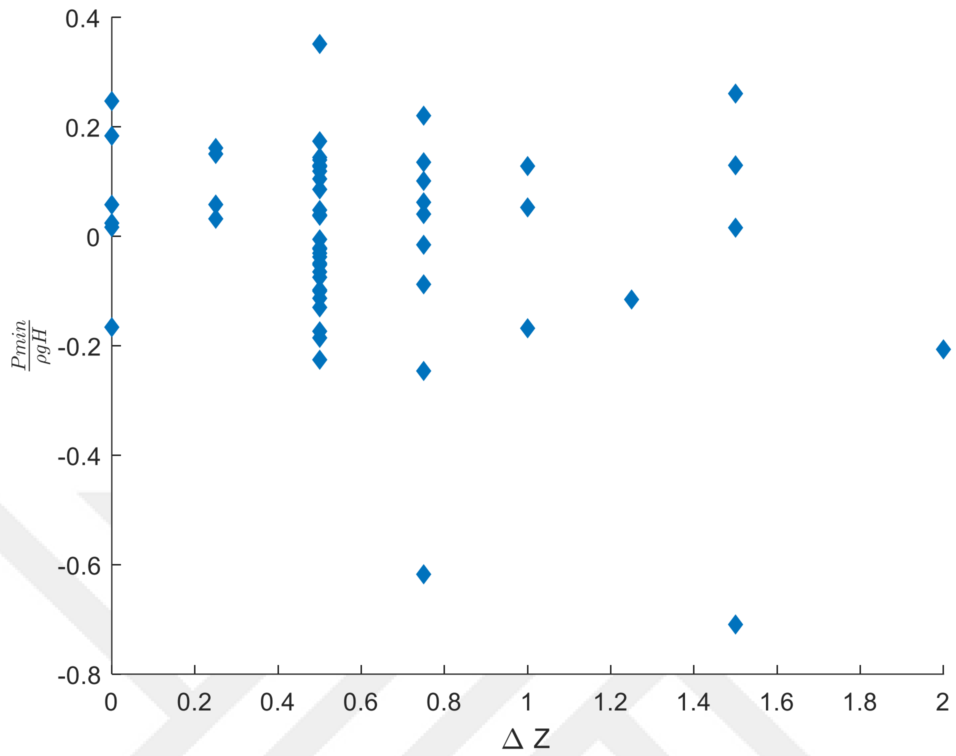

Figure 4.16: ΔZ vs $P_{min}/\rho g H$ for individual waves with double-peaked hydrodynamic loading

When the above given four figures (Figure 4.13, 4.14, 4.15 and 4.16) are considered, a meaningful relation cannot be proposed, especially for ΔX included graphs. For ΔZ included graphs, there are several outlier data points and these make it difficult to draw a meaningful results but accumulations of the data points are mclearerthan the accumulations data points in ΔX included graphs. Nevertheless, the relation between minimum value of the first peak and ΔX - ΔZ parameters cannot be figured out. If there were higher ranges of ΔX and ΔZ parameters or there were more than one pressure sensors, it would have been possible make an inference.

In order to observe the relation between and absolute differences of maximum and minimum values of first peak of the individual waves that have double-peaked hydrodynamic loading after wave breaking and ΔX- ΔZ, below given figures (Figure 4.17, 4.18, 4.19 and 4.20) are plotted. ΔP parameter was non-dimensionalized by dividing ρ, g and corresponded h and H values.

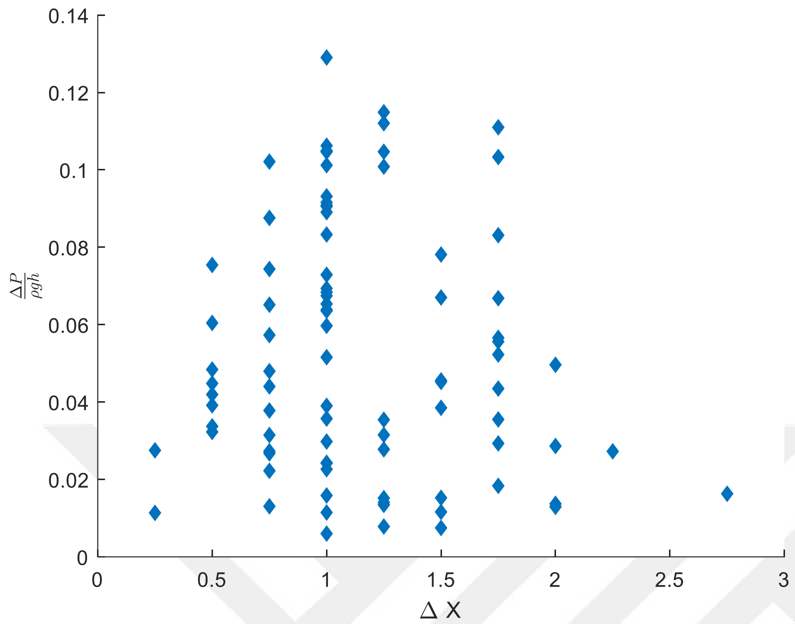

Figure 4.17: ΔX vs $\Delta P/\rho g h$ for individual waves with double-peaked hydrodynamic loading

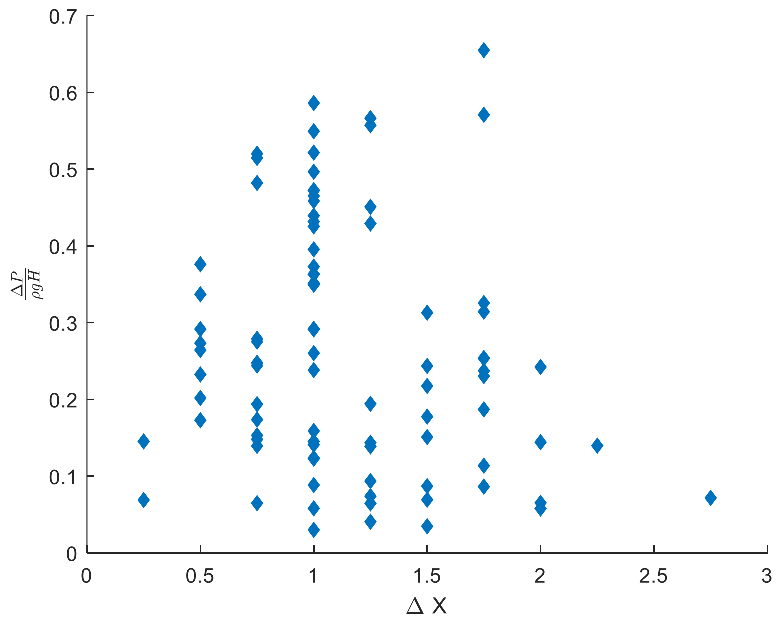

Figure 4.18: ΔX vs $\Delta P/\rho g H$ for individual waves with double-peaked hydrodynamic loading

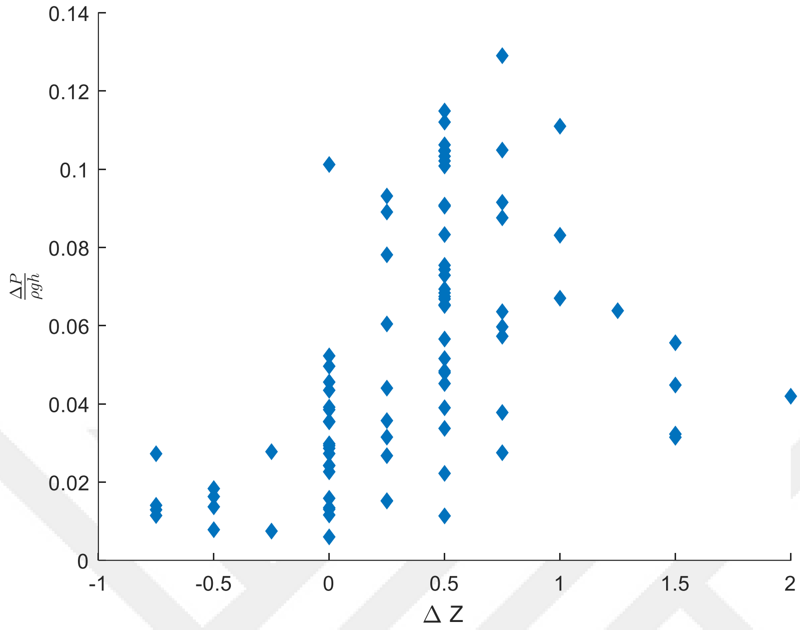

Figure 4.19: ΔZ vs $\Delta P/\rho g h$ for individual waves with double-peaked hydrodynamic loading

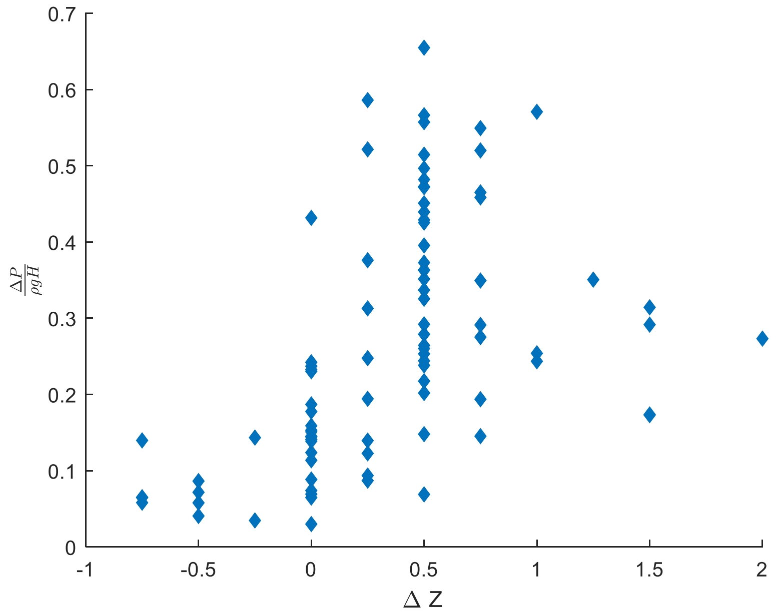

Figure 4.20: ΔZ vs $\Delta P/\rho g H$ for individual waves with double-peaked hydrodynamic loading

When the above given four figures (Figure 4.17, 4.18, 4.19 and 4.20) are considered, again a meaningful relation cannot be proposed. If there were higher ranges of ΔX and ΔZ $parameters$ or there were more than one pressure sensors, it would have been possible to make an inference.

In order to observe the relation between and minimum first peak pressure values of the individual waves that have double-peaked hydrodyanmic loading after wave breaking and $T\sqrt{gH}/h$ non-dimensional parameter, below given figures (Figure 4.21 and 4.22) are plotted. In Figure 4.21, P_{min} parameter was non-dimensionalized by dividing ρ, g and corresponded h, and in Figure 4.22 P_{min} parameter was non-dimensionalized by dividing ρ, g and corresponded H values.

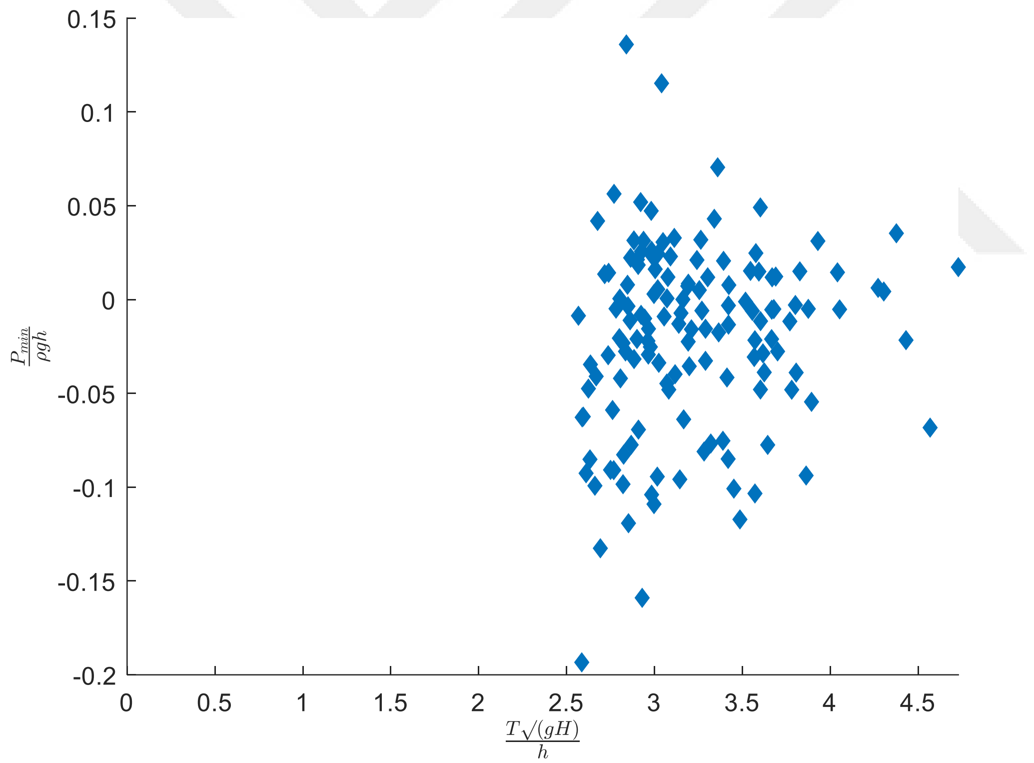

Figure 4.21: $T\sqrt{gH}/h$ vs $P_{min}/\rho gh$ for individual waves with double-peaked hydrodynamic loading

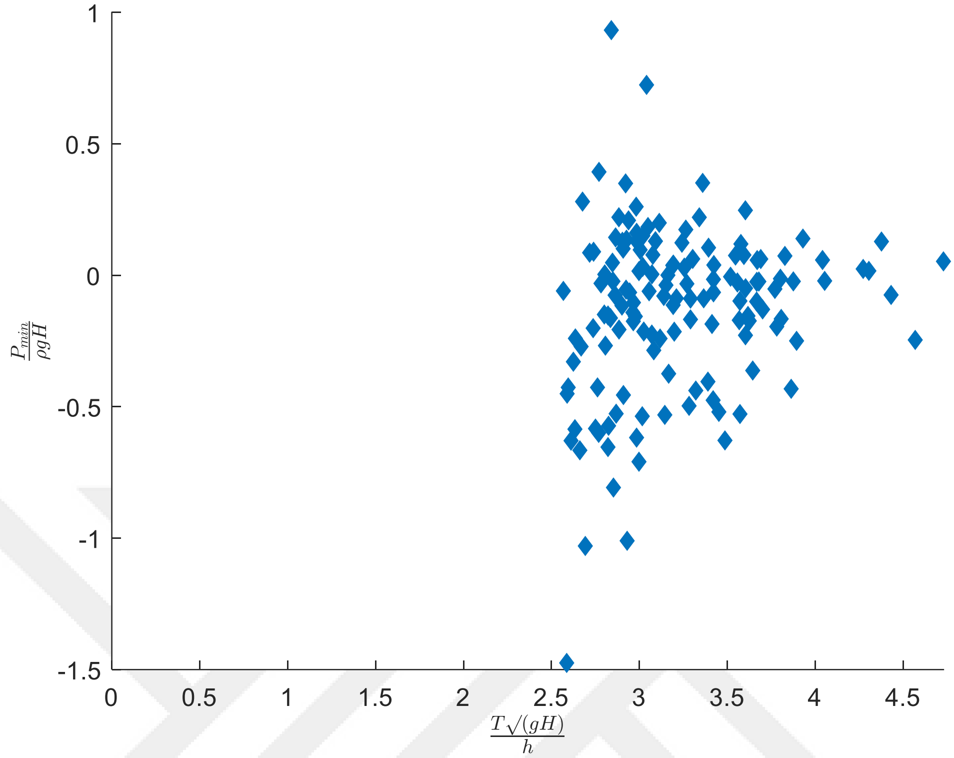

Figure 4.22: $T\sqrt{gH}/h$ vs $P_{min}/\rho gH$ for individual waves with double-peaked hydrodynamic loading

When the results in Figure 4.21 and Figure 4.22, it can be stated that when $T\sqrt{gH}/h$ value increases, number of occurrences of the signal-peaked type hydrodynamic loading decreases. This result can be given as a meaningful inference according to Figure 4.21 and Figure 4.22.

In order to observe the relation between and absolute differences of maximum and minimum values of first peak of the individual waves that have double-peaked hydrodyanmic loading after wave breaking and $T\sqrt{gH}/h$ non-dimensional parameter, below given figures (Figure 4.23 and 4.24) are plotted. In Figure 4.23, ΔP parameter was non-dimensionalized by dividing ρ, g and corresponded h, and in Figure 4.24, ΔP parameter was non-dimensionalized by dividing ρ, g and corresponded H values.

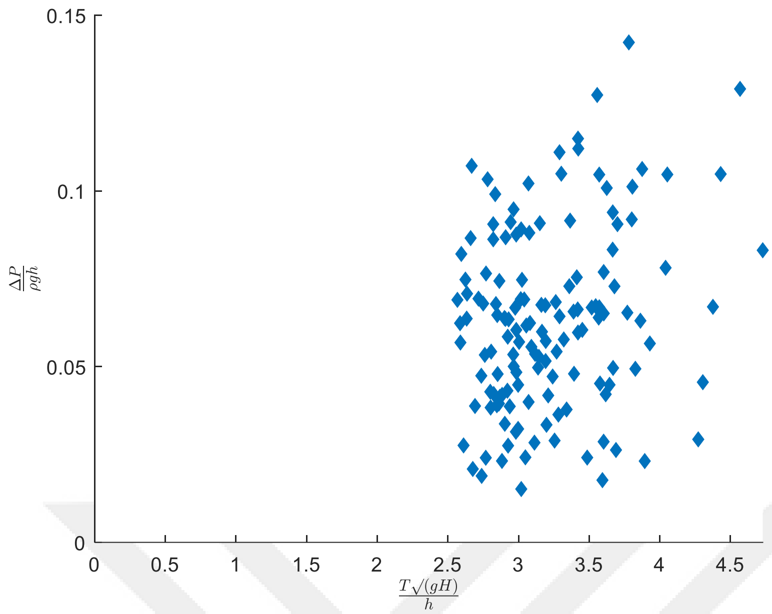

Figure 4.23: $T\sqrt{gH}/h$ vs $\Delta P/\rho g h$ for individual waves with double-peaked hydrodynamic loading

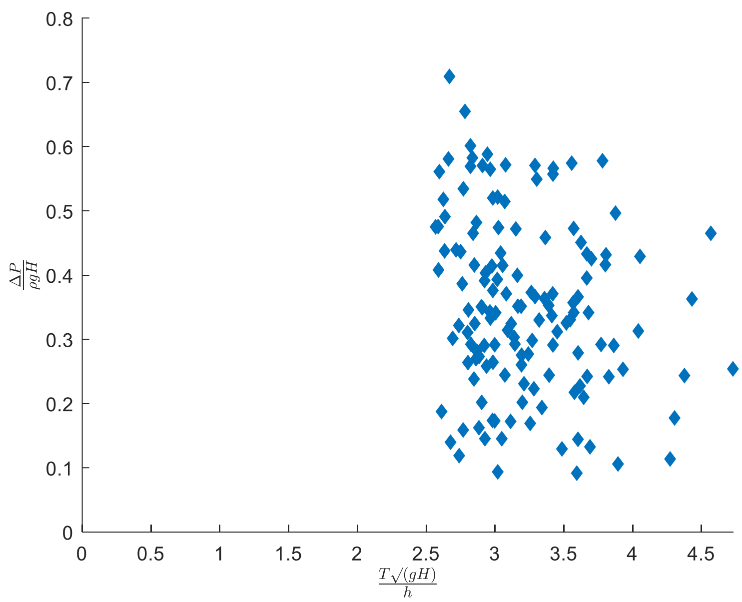

Figure 4.24: $T\sqrt{gH}/h$ vs $\Delta P/\rho g H$ for individual waves with double-peaked hydrodynamic loading

Like the previous graphs (Figure 4.21 and Figure 4.22), when the results in Figure 4.23 and Figure 4.24 are considered, it can be stated that c value increases, number of occurrences of the signal-peaked type hydrodynamic loading decreases. This result can be given as a meaningful inference according to Figure 4.23 and Figure 4.24. Furthermore, it can also be stated that when $T\sqrt{gH}/h$ value increases, $\Delta P/\rho gH$ value decreases.

In order to observe the relation between Keulegan – Carpenter (KC) number with ΔX-ΔZ parameters, Figure 4.25 and Figure 4.26 are plotted.

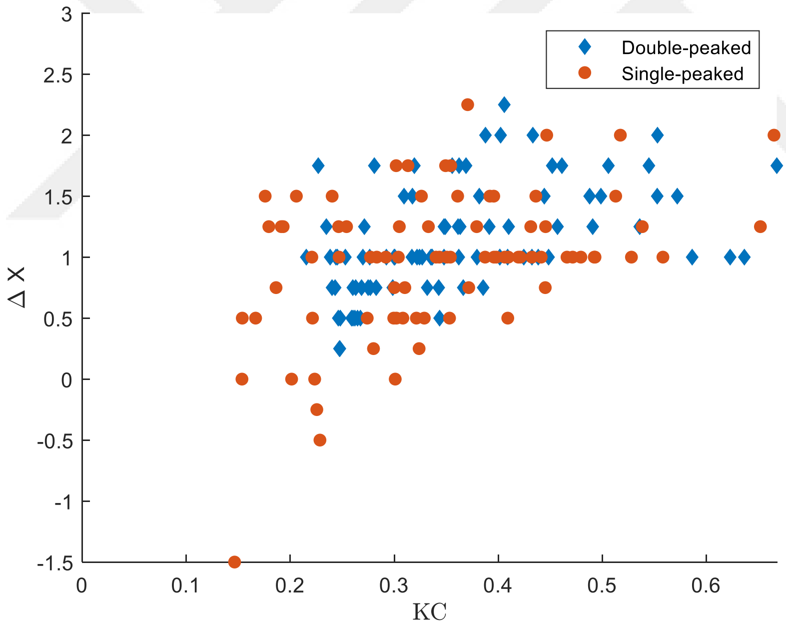

Figure 4.25: KC vs ΔX

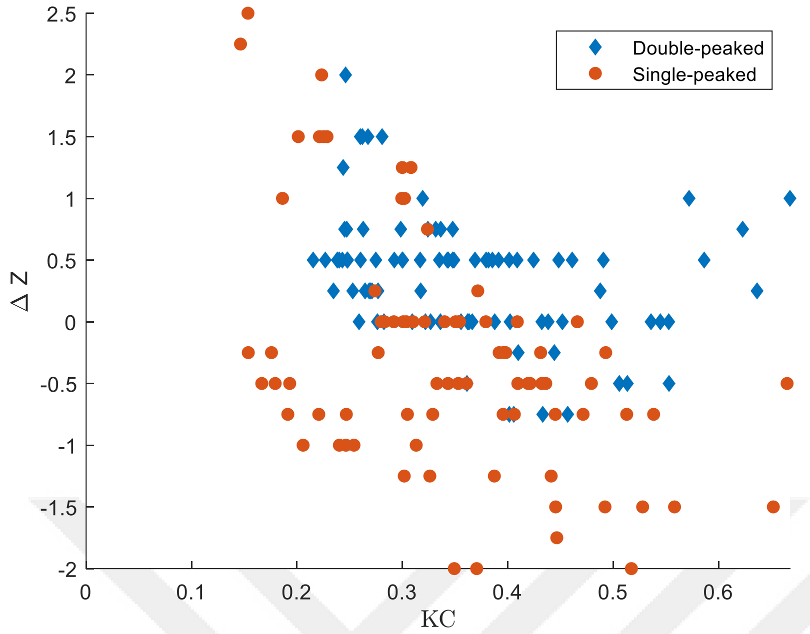

Figure 4.26: KC vs ΔZ

According to the Figure 4.25 and Figure 4.26, it is seen that the individual wave that have single-peaked type hydrodynamic loading have a wider range in terms of KC parameter than the the individual wave that have double-peaked type hydrodynamic loading.

In order to observe the relation between ΔX and ΔZ values waves that have both single peak and double peak types hydrodynamic loading, Figure 4.27 was plotted. As it can be seen from this figure, waves that have single peak and double peak types hydrodynamic loading, accumulated seperately. From this result, it can be stated that according to the breaking point of the plunger with respect to the pressure sensor, waves create different hydrodynamic loading types. According to Figure 4.27, to observe a double peak hydrodynamic loading, plunger should break before the pressure sensor, in other words, circumferential distance of unit width offshore should be positive, but there is not such a case to see a single peak type hydrodynamic loading. This type of hydrodynamic loading can be seen for breaking points which are before or after the pressure sensor, which means this type of loading can be seen for both positive and negative values of ΔX.

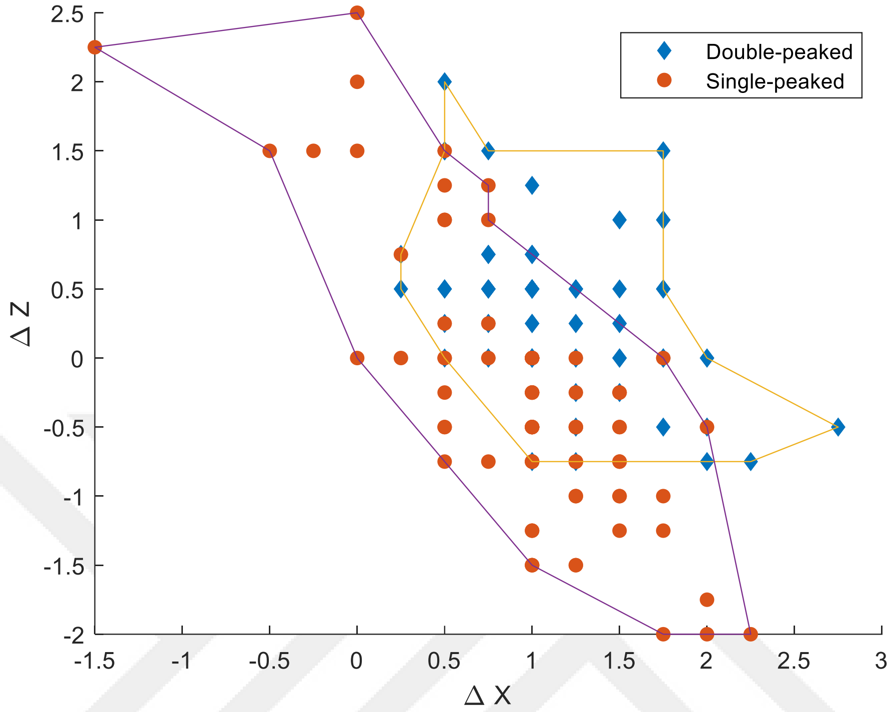

Figure 4.27: ΔX vs ΔZ for individual waves with both single-peaked and double-peaked hydrodynamic loading

When the ΔZ values are compared, it is seen that waves that have single peak type hydrodyanmic loading have a larger range than the waves that create double peak hydrodynamic loading on the pressure sensor. Another important point is that the results show a transition area between single-peaked type hydrodynamic loading and double-peaked type hydrodynamic loading. The range of this transition area can be defined as between of -0.75 and 0.25 for ΔZ and between of 0.25 and 1.75 for ΔX. Thus, the effect of the location of the wave breaking on the type of hydrodynamic loading is relatively understood.

In Figure 4.28, a 3D bar plot is presented to show the relation between ΔP and location of the breaking of the plunger in terms of both ΔZ and ΔX. In Figure 4.29 a 3D bar plot is presented to show the relation between P_{min} and ΔZ-ΔX.

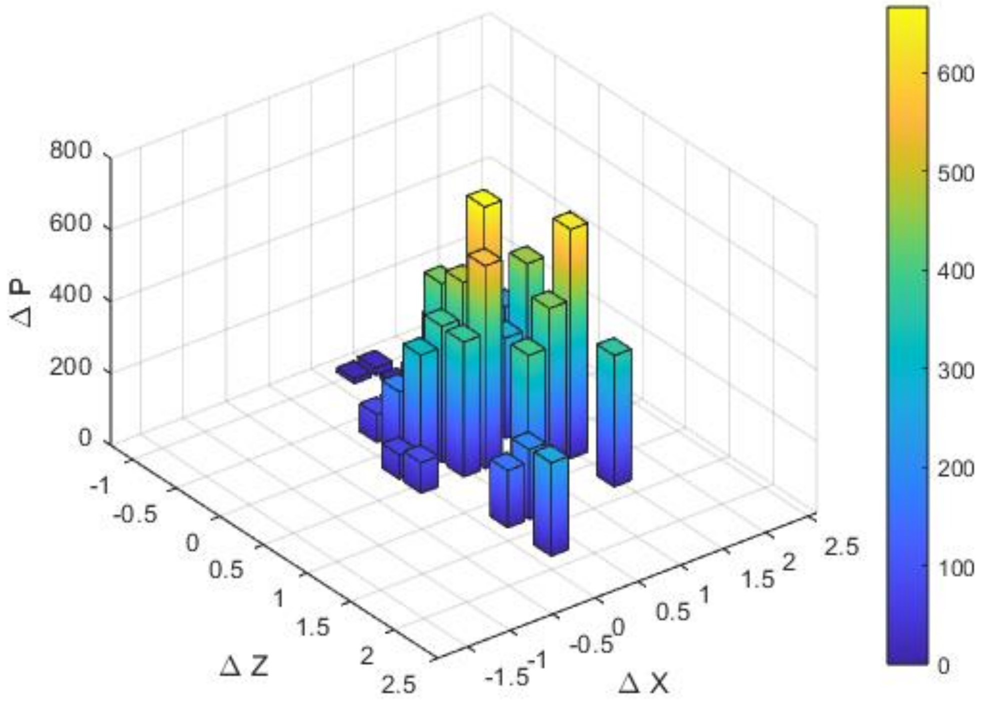

Figure 4.28: 3D Bar plot of ΔZ-ΔX vs ΔP

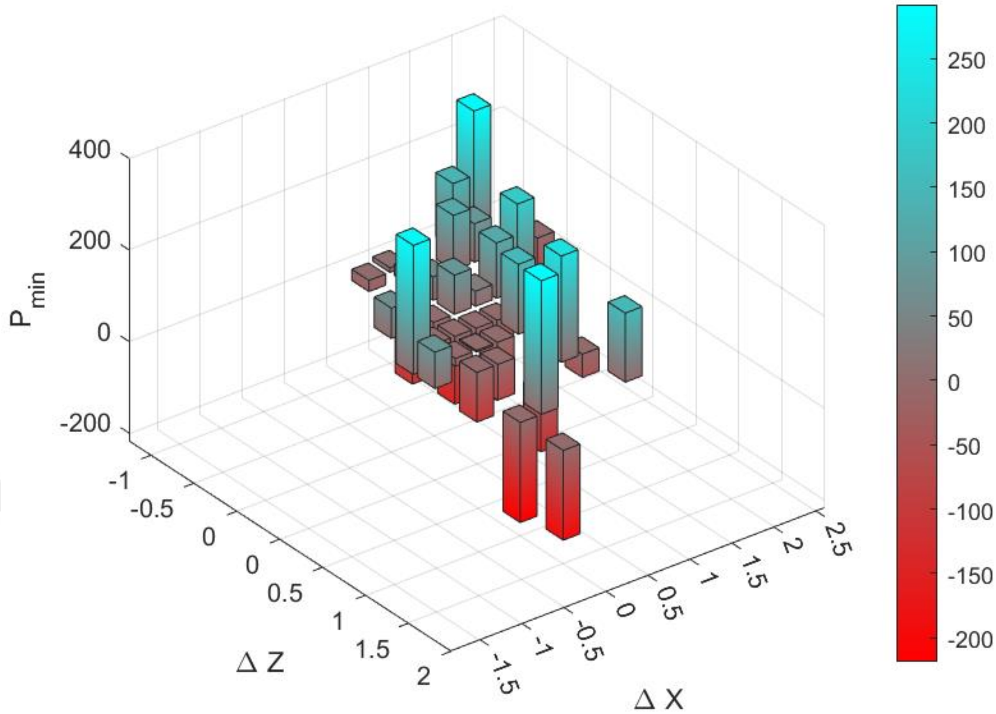

Figure 4.29: 3D Bar plot of ΔZ-ΔX vs P_{min}

When Figure 4.28 is considered, it can be stated that absolute difference between the first peak and first minimum points of the double-peaked type hydrodynamic loading increases when ΔZ and ΔX values get their average values or close values to their average values of their ranges for double-peaked occurrence situation.

When Figure 4.29 is considered, it is not possible to state a meaningful result for occurance of negative and positive minimum pressure values of the first peak of the double-peaked type, in a specific range for ΔZ and ΔX.

In Figure 4.30, a relation between $\Delta Za/H$ and $\Delta Xa/L$ non-dimensional parameters. Due to the lack of data points and spread of the existing data points on a large range, there is not a chance to make a meaningul inference for single-peaked type data. If a few outlying data points are ignored, double-peaked type data points accumlate in the range of 0-40 for $\Delta Za/H$ paraemeter and 1-2.25 for $\Delta Xa/L$ parameter . But, there is not a chance to make a clear inference, in general.

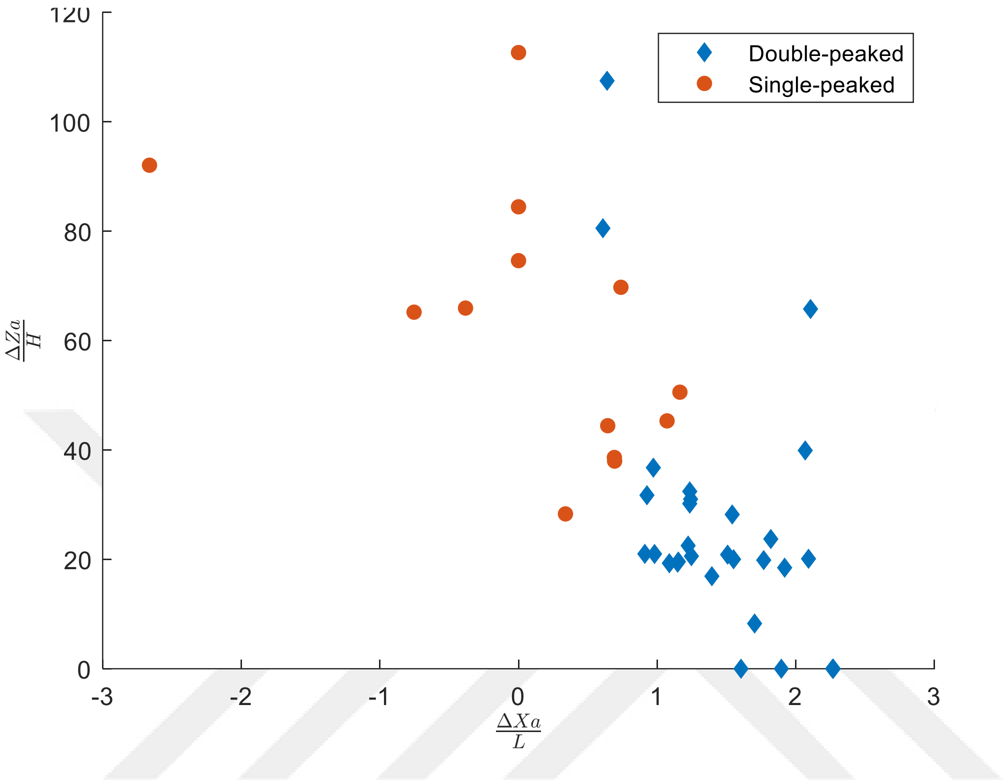

Figure 4.30: $\Delta Za/H$ vs $\Delta Xa/L$

To sum up the formation processes of wave breaking and corresponded hydrodynamic loading, local vortex formation near the pressure sensor is the reason why the hydrodynamic loading is of double-peaked type. The factor influencing the vortex formation near the pressure sensor and the subsequent passage of the vortex over the pressure sensor is the position of the wave breaking relative to the pressure sensor. Single-peaked type hydrodynamic loading is observed when the wave breaks very close to the pressure sensor, directly above it or after it passed the sensor. In this case, the vortex will form at a point further away from the pressure sensor, so there will be only a single maximum and minimum pressure values in single-peaked type hydrodynamic loading.

When the wave breaking occurs before it reaches the pressure sensor and will be even larger as it passes over the pressure sensor, so there will be extra maximum and minimum pressure values at the hydrodynamic loading graph due to the suction force caused by the vortex. According to the results that were found in the scope of this thesis study, average wave breaking locations relative to the pressure sensor is 0.61 ΔZ and 1.08 ΔX for double-peaked type, 1.14 ΔZ and 0.12 ΔX for single-peaked type.

72

CHAPTER 5

CONCLUSION

In the scope of this thesis study, physical model experiments were carried out based on a physical model of a real-life rubble mound breakwater head section to have a deeper understanding of the relation between the hydrodynamic loading due to wave breaking on the lee-side of the rubble mound breakwater head section and wave parameters such as wave breaking type, individual wave height, individual wave period and so on. These relations were studied utilizing water surface elevation, velocity and pressure measurements in addition to video records during the experiments. In this section of this thesis study, the conclusions of the study and recommendations for further studies are given.

When the results of the experiments are considered, several significant findings can be mentioned. These findings can be summaried as follows.

- According to the results, during the passage of a single wave, hydrodynamic loading on a single antifer unit changes remarkably depending on the presence and location of wave-breaking. Two types of hydrodynamic loading were observed in the measurements, these types are named as single-peaked and double-peaked.
- When the wave breaking and breaking-induced vortex formation occurs before they reach the pressure sensor, there will be extra maximum and minimum pressure values at the hydrodynamic loading graph besides the main peak and minimum values that are observed in the single-peaked type, due to suction force caused by the vortex.
- It is observed that the pressure signal on the top face of the unit takes a double-peaked form rather than single-peaked with strong negative dynamic

pressure values when the plunger breaks at an average circumferential distance of 1.08 unit width offshore and vertical distance of 0.61 unit width above.

- According to the results, absolute difference between the first peak and first minimum points of the double-peaked type hydrodynamic loading increases when ΔZ and ΔX values gets close to their average values of their ranges for double-peaked occurance situation. A relationship between minimum pressure values of the first peak of the double-peaked hydrodynamic loading with ΔZ and ΔX values cannot be established.
- According to particle velocity measurement results at six different measurement points, velocities significantly increase when measurement point get closer to the lee-side of the head section up to four times the undisturbed values for a 1.8 s wave period case and up to three times the undisturbed values for 1.9 s wave period case.

When research questions that are given in the Introduction part are considered, according to the results, an answer can be given for how the location of wave breaking effectaffects the hydrodynamic loading on the lee-side of the head section of the rubble mound breakwater, is given. However, due to the range of the studied wave period and wave height values, a clear relation between wave parameters and wave load and pressure acting on the lee-side of the head section of a rubble mound breakwater, cannot be given. In addition to this situation, an explanation for how hydrodynamic loading changes is given according to the wave breaking locations not according to the changing wave parameters.

After the concluding remarks, suggestions for further studies should be given. In the scope of this study, physical model experiments were conducted with the same approach angle of propagating waves, armor layer slope, alignment of the head section, and type of artificial armor layer unit. During the experiments, two gauges and a single pressure sensor were used at the same locations for all tests. In order to further develop this study and to observe the effects of hydrodynamic loading on the antifer concrete block armor layer units after wave breaking phenomenon on the lee-side of the head section of a rubble mound breakwater over a wider observing area, developing and modifying physical model that was constructed in the scope of this study may be required. These developments and modifications for the experimental setup are given below as a list:

- In the experiments, almost all of the observed wave-breaking types are the same as the 'plunging type'. A variety of wave steepness values or structure slopes can be studied to observe other wave-breaking types and their effects on the type and magnitude of the hydrodynamic loading, for further studies.
- During the experiments, a single pressure sensor was located on the physical model. Increasing the number of pressure sensors and the variety of the locations of the pressure sensor may give a chance to have a deeper understanding of the hydrodynamic loading and its changes according to the location of wave breaking on the head section of rubble mound breakwater. In addition, locating the pressure sensor on the transition section where is the region between the head section and the trunk section on the harbor side of the physical model may give valuable information.
- In the experiments, an already existing physical model of a rubble mound breakwater head from a real-life project with bathymetry was used. The head design and the placement of the head in the flume are not generic. During the construction of the physical model, the same alignment of the head section to the trunk section was modeled to be the same as the real-life rubble mound breakwater. This degree of alignment with respect to the trunk section can be changed and the effect of the alignment of the head section can be observed.
- In this thesis study, Acoustic Doppler Velocimetry (ADV) measurements were taken at 6 different points for selected test cases. The number of locations of ADV measurement points and test cases can be increased to determine the change of velocity of propagating waves for different locations around the physical model.

- In the scope of this study, only antifer concrete block armor layer units were used for the armor layer of the rubble mound breakwater model. For further studies, different types of units for instance rock, tetrapod, Xbloc, and so on can be tested to observe the relation between hydrodynamic loading after wave breaking and the type of armor layer unit.
- Finally, in addition to physical model experiments, numerical model studies can also be conducted in the scope of this topic. A constructed physical model of the head section or a generic one can be modeled in a computational fluid dynamics (CFD) numerical model, for instance, OpenFOAM, and a wider range of wave and structure conditions can be tested in these numerical model studies and in this way, a more comprehensive study can be carried out.

REFERENCES

Brocchini, M., Marini, F., Postacchini, M., Zitti, G., Falchi, M., & Xie, Z. (2022). Interaction between breaking-induced vortices and near-bed structures. Part 1. Experimental and theoretical investigation. *Journal of Fluid Mechanics*, *940*, A44.

Chang, K. A., Hsu, T. J., & Liu, P. L. F. (2001). Vortex generation and evolution in water waves propagating over a submerged rectangular obstacle: Part I. Solitary waves. *Coastal Engineering*, *44*(1), 13-36.

Chang, K. A., Hsu, T. J., & Liu, P. L. F. (2005). Vortex generation and evolution in water waves propagating over a submerged rectangular obstacle: Part II: Cnoidal waves. *Coastal Engineering*, *52*(3), 257-283.

Eden, D., Douglas, S., Simpalean, A., Kozlowski, T., Nistor, I., Cornett, A., ... & Tabarestani, M. K. (2019). Quantifying Forces and Pressures on Core-Loc™ Armour Units via Instrumented Units and Image Processing. In *Coastal Structures Conference 2019* (pp. 2-11).

Fredsøe, J., & Sumer, B. M. (1997). Scour at the round head of a rubble-mound breakwater. *Coastal Engineering*, *29*(3-4), 231-262.

Govindasamy, V. K., Chella, M. A., Annamalaisamy, S. S., & Rajamanickam, P. S. (2023). Impact pressure distribution and characteristics of breaking wave impact on a monopile. *Ocean Engineering*, *271*, 113771.

Iwata, K., Miyazaki, Y., & Mizutani, N. (1985). Experimental study of the wave force acting on armour rubble of a rubble-mound slope. *Natural disaster science*, *7*(2), 29-41.

Kim, S. Y., Kim, K. H., & Kim, Y. (2015). Comparative study on pressure sensors for sloshing experiment. *Ocean Engineering*, *94*, 199-212.

Kowalewski, M. J. (1994). *Quality and statistics: total quality management* (Vol. 1209). ASTM International.

Lee, G. N., Jung, K. H., Malenica, S., Chung, Y. S., Suh, S. B., Kim, M. S., & Choi, Y. H. (2020). Experimental study on flow kinematics and pressure distribution of green water on a rectangular structure. *Ocean Engineering*, *195*, 106649.

Losada, M. A., Medina, R., & Alejo, M. (1988). Wave forces on armor blocks. In *Coastal Engineering 1988* (pp. 2479-2488).

Nadaoka, K., Hino, M., & Koyano, Y. (1989). Structure of the turbulent flow field under breaking waves in the surf zone. *Journal of Fluid Mechanics, 204,* 359-387.

Sandstrom, A. (1974). *Wave forces on blocks of rubble-mound breakwaters*. Royal Institute of Technology.

Sakakiyama, T., & Kajima, R. (1990). Scale effect of wave force on armor units. In *Coastal Engineering 1990* (pp. 1716-1729).

Sumer, B. M., Guner, H. A. A., Hansen, N. M., Fuhrman, D. R., & Fredsøe, J. (2013). Laboratory observations of flow and sediment transport induced by plunging regular waves. *Journal of Geophysical Research: Oceans*, *118*(11), 6161-6182.

Tørum, A. (1994). Wave-induced forces on armor unit on berm breakwaters. *Journal of waterway, port, coastal, and ocean engineering*, *120*(3), 251-268.

van Gent, M. R. (2014). Oblique wave attack on rubble mound breakwaters. *Coastal Engineering*, *88*, 43-54.

Williams, B., Lacy, P. S., Yan, P., Hwee, C. N., Liang, C., & Ting, C. M. (2011). Development and validation of a novel method to derive central aortic systolic pressure from the radial pressure waveform using an N-point moving average method. *Journal of the American College of Cardiology*, *57*(8), 951-961.

Williamson, D. C., & Hall, K. R. (1992). Prediction of external wave pressures on a rubble mound breakwater. *Canadian Journal of Civil Engineering*, *19*(4), 639-648.

Wise, L. (1999). Numerical and physical modeling of wave forces on A-Jacks units.

Zaeni, A., Kasnalestari, T., & Khayam, U. (2018, October). Application of wavelet transformation symlet type and coiflet type for partial discharge signals denoising. In *2018 5th International Conference on Electric Vehicular Technology (ICEVT)* (pp. 78-82). IEEE.

Zhang, D. P., & Sunamura, T. (1994). Multiple bar formation by breaker-induced vortices: a laboratory approach. In *Coastal Engineering 1994* (pp. 2856-2870).

APPENDICES

A. Signal Filtering

After the completion of the physical experiment phase, obtained water surface elevation, pressure, and velocity measurement data were investigated. It was determined that there is noise in almost all the pressure and velocity measurements at different levels. To get rid of this noise from the obtained measurements, different signal-denoising methods were applied to these pressure measurements to determine the de-noised time-series from the measurements. These methods are classified into three groups which are low-pass filters, wavelet transforms, and moving average methods.

Low-pass filters are used to pass the signals that have a lower frequency than the determined cut-off frequency value and eliminate the signals that have a higher frequency than the determined cut-off frequency value. In the scope of this study, as low-pass filters, Butterworth, Chebyshev, Bessel, and finite impulse response (FIR) filters were used with different orders. Low pass filters have two types which are analog and digital. In this thesis study, analog-type filtering was used for all three low-pass filters. While using analog-type low-pass filtering, filter order and cut-off frequency values were needed. Orders of these low-pass filters were selected according to the methodology that is given in the study of Lee et al. (2019) which is also given in Chapter 2, literature review part. The cut-off frequency was determined as 45 Hz for all sampling frequencies of measured data according to the background noise frequency component in the frequency spectrums.

The wavelet transformation is a developed version of the Fourier transform and it gives a chance to divide a signal into its all frequency components since it is a conversion function thus, these frequency components can be studied separately. The wavelet transform can give the frequency and time domains of a signal simultaneously (Zaeini et al., 2018). Signal filtering of the pressure measurements was carried out by using the Wavelet Analyzer Toolbox of MATLAB R2022a. There are several types of wavelet transformation and eight types are listed below.

- Coiflet wavelet (Coif)
- Symlet wavelet (Sym)
- Haar wavelet (Haar)
- Daubechies wavelet (Db)
- Fejer-Krovkin wavelet (Fk)
- Biorthogonal Spline wavelet (Bior)
- Reverse Biorthogonal Spline wavelet (Rbio)
- Discrete approximation of Meyer Wavelet (Dmey)

For the above-given wavelet types, different orders but the same levels, which are 10 and 11, were selected according to a trial-and-error process to prevent excessive smoothing of the measured signal by making a visual comparison.

The third method to eliminate the background noise is the moving average method. The moving average method is a widely used mathematical method in applications of various disciplines for data smoothing to observe underlying trends (Williams et al., 2011). The moving average method acts like a low-pass filter in data smoothing and a data window of 1250 data points was used for implementation of this method in the scope of this thesis study. The data window range was determined according to a trial-and-error process to prevent excessive smoothing of the measured signal by making a visual comparison as same as with wavelet transform methods.

There were different sampling frequency values were used during pressure measurements in the scope of this thesis study. A sampling frequency of 12.5 kHz for 11 wave sets, a sampling frequency of 25 kHz for three wave sets, a sampling frequency of 31.25 kHz for five wave sets, and a sampling frequency of 62.5 kHz for 91 wave sets was applied. Before the signal-filtering process, because of the different sampling frequency values for pressure measurements, the down-sampling process was applied to pressure measurement outputs that were not recorded with a sampling frequency of 12.5 kHz. The underlying reason for this situation is both to use all the pressure measurement results that were obtained and to obtain more uniform results by bringing these results to the same sampling frequency. It is noted that for impact pressure measurements it is suggested to use sampling frequencies of more than 10 kHz (Wienke & Oumeraci, 2005), which supports the selection of the sampling frequency in the present study. After the completion of the down-sampling process, the signal-filtering process was conducted for all pressure measurement results. An example of the filters that are plotted on the raw pressure data is given in Figure A.1.

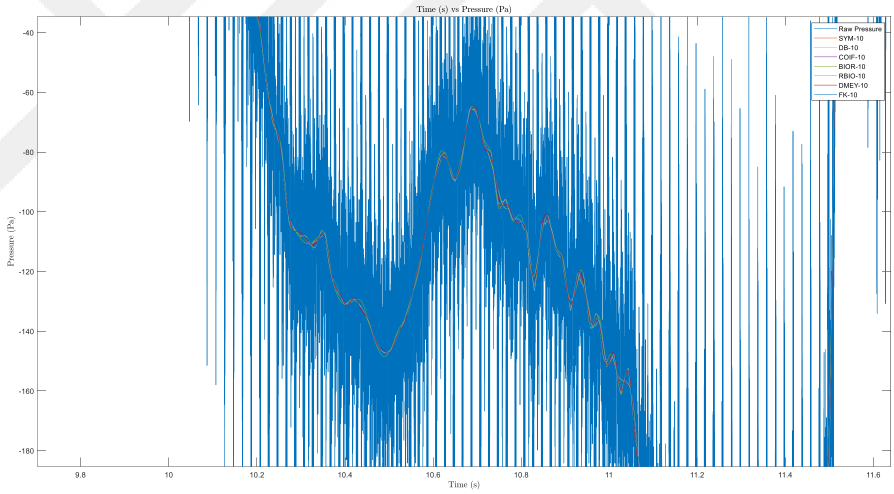

Figure A.1: Example of filters on raw pressure data

B. Statistical Analysis for Signal Filtering

As it is mentioned in Chapter 3, different signal-denoising methods were applied to pressure measurements. To determine the best method for pressure measurements, a two-stage approach was followed. As a first step, the results of all the applied signal-denoising methods were plotted on the raw signal and visually compared, and the degree and level of each method that gave the best results were used in the second evaluation stage.

In the second stage, the best level and degree of each signal-denoising method were subjected to error analysis with the help of different statistical methods and thus the best signal-denoising method was selected. The applied statistical methods for error analysis are listed below:

- Mean Squared Error (MSE)
- Normalized Mean Squared Error (N-MSE)
- Scatter Index (SI)
- BIAS
- Normalized BIAS (N-BIAS)
- Mean Absolute Error (MAE)
- Normalized Mean Absolute Error (N-MAE)
- Linear Correlation Coefficient (R)

The above-given methods were chosen according to their different perspectives on error computation and their different explanation for the agreement between the measured and predicted values. Information about the statistical methods named above and the equations used are given in the following sections. In the below-given equations, the letter D refers to denoised data, the letter M refers to measured data in the experiments, and the letter N refers to the amount of data.

1 - Mean Squared Error (MSE) and Normalized Mean Squared Error (N-MSE)

Mean Squared Error (MSE) is one of the most applied apply methods in statistical analysis. To apply this method, the square of differences of denoised and measured data were summed up and the average of this value was found. Normalized mean squared error is found by dividing the MSE value by the multiplication of mean values of measured and denoised data. Lower values of MAE and N-MAE mean higher accuracy. Formulations of both methods are given below (Eq.B.1, Eq.B.2, Eq.B.3, and Eq.B.4).

$$MSE = \frac{1}{N}\sum_{i=1}^{N}(D_i - M_i)^2 \tag{B.1}$$

$$N - MSE = \frac{\sum_{i=1}^{N}(D_i - M_i)^2}{\bar{D} * \bar{M}} \tag{B.2}$$

$$\bar{M} = \frac{1}{N}\sum_{i=1}^{N} M_i \tag{B.3}$$

$$\bar{D} = \frac{1}{N}\sum_{i=1}^{N} D_i \tag{B.4}$$

2 - BIAS and Normalized BIAS (N-BIAS)

BIAS can be defined as a systematic error and the difference between a population mean of the carried-out measurements or test results and a true value or an accepted reference (Kowalewski, 1994). BIAS can be both positive and negative. When it is positive, it means that there is an underestimation and when it is negative, there is an overestimation. N-BIAS is the normalized version of the BIAS and it can be calculated by dividing BIAS values with the summation of the measured values. Lower absolute values of BIAS and N-BIAS mean higher accuracy. Formulations that are used to calculate BIAS and N-BIAS values are given below in Eq.B.5 and Eq.B.6, respectively.

$$BIAS = \frac{1}{N}\sum_{i=1}^{N}(M_i - D_i) \tag{B.5}$$

$$N - BIAS = \frac{\sum_{i=1}^{N}(M_i - D_i)}{\sum_{i=1}^{N} M_i} \tag{B.6}$$

3 - Mean Absolute Error (MAE) and Normalized Mean Absolute Error (N-MAE)

Mean Absolute Error (MAE) is one of the most applied and easy-to-apply methods. To apply this method, absolute differences of denoised and measured data were summed up and the average of this value was found. Normalized mean absolute error is found by dividing the MAE value by the standard deviation of measured values. Lower values of MAE and N-MAE mean higher accuracy. Formulations of both methods are given below (Eq.B.7 and Eq.B.8).

$$MAE = \frac{1}{N}\sum_{i=1}^{N}|D_i - M_i| \tag{B.7}$$

$$N - MAE = \frac{MAE}{S} \tag{B.8}$$

S represents the standard deviation of measured values and the formulation of it is given below (Eq.B.9). $\overline{M}$ represents the average of the measured values and it is a parameter in the standard deviation equation (Eq.B.9). It is also given below (Eq.B.10).

$$S = \sqrt{\frac{1}{N-1}\sum_{i=1}^{N}|M_i - \bar{M}|} \tag{B.9}$$

$$\bar{M} = \frac{1}{N}\sum_{i=1}^{N} M_i \tag{B.10}$$

4- Scatter Index (SI)

Scatter Index (SI) is another statistical analysis method to calculate the percentage of difference of the root mean squared error (RMSE) with respect to the average value of the measured data. It can be found by dividing the root mean squared error (RMSE) value that is calculated by using measured and denoised data, with the average of the measured data values. The formulations of scatter index (SI) and root mean squared error (RMSE) are given below in Eq.B.11 and Eq.B.12, respectively.

$$SI = \frac{RMSE}{\bar{M}} \tag{B.11}$$

$$RMSE = \sqrt{\frac{1}{N}\sum_{i=1}^{N}(D_i - M_i)^2} \tag{B.12}$$

Lower values of the Scatter Index mean higher performance of the used method for prediction.

5- Linear Correlation Coefficient (R)

Another statistical analysis method used to measure the accuracy between two different data is the Linear Correlation Coefficient (Pearson, 1895). This method was used to determine the linear correlation between the filtered and measured data. The below-given equation (Eq.B.13) was used to measure this linear correlation.

$$R = \frac{\sum_{i=1}^{N}\left(D_i - \bar{\bar{D}}\right) * \left(M_i - \bar{\bar{M}}\right)}{\sqrt{\sum_{i=1}^{N}\left(D_i - \bar{\bar{D}}\right)^2 * \sum_{i=1}^{N}\left(M_i - \bar{\bar{M}}\right)^2}} \qquad \text{(B.13)}$$

This coefficient takes values between -1 and 1. When R = 1, it means there is a full correlation between the two data sets. When 'R' equals 0, this means that there is no correlation between the two data sets. When 'R' equals -1, this means that there is a negative full correlation between data sets. In other words, if variables of one data set tend to increase, variables of another data set tend to decrease.

During the analysis part, two of the pressure measurement data were selected, and the pressure signals of three individual waves which are not affected by wave reflection in the wave flume were filtered with the above-given signal filtering methods separately for each data After this process, above listed statistical analysis tools were applied to the pressure signals of six individual waves. When the results of these statistical tools were evaluated, SI, BIAS, N-BIAS, and R methods gave almost the same results for all signal filtering methods and due to this situation, the decision to choose the most appropriate signal filtering type was made by looking at the results of MAE, N-MAE, MSE, N-MSE statistical analysis methods.

In the below given table below (Table B.1), determined orders and levels for chosen signal filtering methods. As mentioned in Chapter 3, the order of the low-pass filters was determined according to the method that was proposed in the study by Lee et al. (2019). During the determination of the order of chosen low-pass filters, conditions that are given by (Eq.2.1) and (Eq.2.2) were satisfied. Calculated R_A and R_B values for chosen low-pass filters are given in Table B.2.

In another table given below (Table B.3), results for four selected statistical analysis methods that are applied to the selected signal filtering methods are given for the pressure distribution of an individual wave.

Table B.1: Chosen orders and levels for applied filters

Filters	**Order**	**Level**
BIOR-10	5.5	10
BIOR-11	5.5	11
COIF-10	5	10
COIF-11	5	11
DB-10	10	10
DB-11	10	11
DMEY-10	10	-
DMEY-11	11	-
FK-10	22	10
FK-11	22	11
RBIO-10	5.5	10
RBIO-11	5.5	11
SYM-10	6	10
SYM-11	6	11
BUTTERWORTH-1	3	-
BUTTERWORTH-2	4	-
BUTTERWORTH-3	5	-
FIR-1	200	-
FIR-2	300	-
FIR-3	400	-
FIR-4	500	-
FIR-5	600	-

Table B.2: R_A and R_B values for chosen low-pass filters

Filters	**R_A**	**R_B**
BUTTERWOTH-1	0.9992	0.0050
BUTTERWOTH-2	0.9993	0.0017
BUTTERWOTH-3	0.9956	0.0007
FIR-1	0.9983	0.0825
FIR-2	0.9972	0.0115
FIR-3	0.9959	0.0016
FIR-4	0.9947	0.0010
FIR-5	0.9939	0.0010

In Table B.1, although the moving average method acts like a low-pass filter, chosen order and level values are not given for the moving average method because this method only uses the number of data to be used in a window and this value was chosen as 1250 data points.

In Table B.2, R_A and R_B values for chosen low-pass filters are given and these results show that all chosen low-pass filters with their orders satisfy the methodology that is given in the study of Lee et al. (2019).

Table B.3. Results for statistical analysis

Filters	MSE	N-MSE	MAE	N-MAE
BIOR-10	426.07	$8.71x10^8$	38.75	0.11
BIOR-11	412.47	$9.24x10^8$	40.23	0.11
COIF-10	450.58	$8.63x10^8$	38.73	0.11
COIF-11	421.56	$9.12x10^8$	40.18	0.11
DB-10	453.12	$8.71x10^8$	38.69	0.11
DB-11	448.29	$9.29x10^8$	40.30	0.11
DMEY-10	450.17	$8.55x10^8$	38.73	0.11
DMEY-11	418.35	$9.03x10^8$	40.17	0.11
FK-10	461.92	$8.67x10^8$	38.72	0.11
FK-11	456.09	$9.46x10^8$	40.27	0.11
RBIO-10	454.06	$8.69x10^8$	38.80	0.11
RBIO-11	429.66	$9.34x10^8$	40.40	0.11
SYM-10	450.43	$8.69x10^8$	38.75	0.11
SYM-11	431.96	$9.20x10^8$	40.17	0.11
BUTTERWORTH-1	3297.92	$7.63x10^8$	36.76	0.10
BUTTERWORTH-2	3424.82	$8.21x10^8$	37.46	0.10
BUTTERWORTH-3	3499.34	$8.12x10^8$	37.91	0.11
FIR-1	1776.03	$4.69x10^8$	27.52	0.08
FIR-2	1910.52	$4.97x10^8$	29.58	0.09
FIR-3	2061.51	$5.38x10^8$	31.44	0.09
FIR-4	2189.71	$5.73x10^8$	32.65	0.09
FIR-5	2311.82	$6.02x10^8$	33.21	0.09
MOVING AVERAGE	3623.44	$7.74x10^8$	38.64	0.11

When the results in Table B.3 are considered, it is seen that FIR filters have the best results in the three statistical analysis methods which are N-MSE, MAE, and N-

MAE. Only in the MSE statistical analysis method, wavelet transforms have better results than the low-pass filters and moving average method but in general, FIR filters performed better performance than others. The table shows that the 200th-order FIR filter has the best rating among all FIR filters. However, when this filter is plotted, it can be seen that this degree still captures some background noise in the raw pressure data. Therefore, when all FIR filters were plotted and analyzed, it was decided that it would be most appropriate to use the 400th-order FIR filter for all pressure measurements.